8-1-2017

Spreading Rate-Dependent Variations in Crystallization Along the Global Mid-Ocean Ridge System

V. Dorsey Wanless
Boise State University

Mark D. Behn
Woods Hole Oceanographic Institution

AGU PUBLICATIONS

Geochemistry, Geophysics, Geosystems

RESEARCH ARTICLE
10.1002/2017GC006924

Key Points:
- Crystallization is distributed from the mantle to the seafloor at all ridges, but is enhanced at major thermal and rheologic boundaries
- Peaks in crystallization pressures reflect pooling of magma along the base of the sloping lithosphere and in the shallow melt lens
- The depleted mantle beneath all ridges has relatively uniform CO_2 contents of 50–85 ppm

Supporting Information:
- Supporting Information S1

Correspondence to:
V. D. Wanless,
dwanless@boisestate.edu

Citation:
Wanless, V. D., and M. D. Behn (2017), Spreading rate-dependent variations in crystallization along the global mid-ocean ridge system, *Geochem. Geophys. Geosyst.*, *18*, 3016–3033, doi:10.1002/2017GC006924.

Received 20 MAR 2017
Accepted 1 JUL 2017
Accepted article online 15 JUL 2017
Published online 13 AUG 2017

Spreading rate-dependent variations in crystallization along the global mid-ocean ridge system

V. Dorsey Wanless[1] and Mark D. Behn[2]

[1]Department of Geosciences, Boise State University, Boise, Idaho, USA, [2]Department of Geology and Geophysics, Woods Hole Oceanographic Institution, Woods Hole, Massachusetts, USA

Abstract We investigate crustal accretion at mid-ocean ridges by combining crystallization pressures calculated from major element contents in mid-ocean ridge basalt (MORB) glasses and vapor-saturation pressures from melt inclusions and MORB glasses. Specifically, we use established major element barometers and pressures estimated from 192 fractional crystallization trends to calculate crystallization pressures from >9000 MORB glasses across the global range of mid-ocean ridge spreading rates. Additionally, we estimate vapor-saturation pressures from >400 MORB glasses from PETDB and >400 olivine-hosted melt inclusions compiled from five ridges with variable spreading rates. Both major element and vapor-saturation pressures increase and become more variable with decreasing spreading rate. Vapor saturation pressures indicate that crystallization occurs in the lower crust and upper mantle at all ridges, even when a melt lens is present. We suggest that the broad peaks in major element crystallization pressures at all spreading rates reflects significant crystallization of on and off-axis magmas along the base of a sloping lithosphere. Combining our observations with ridge thermal models we show that crystallization occurs over a range of pressures at all ridges, but it is enhanced at thermal/rheologic boundaries, such as the melt lens and the base of the lithosphere. Finally, we suggest that the remarkable similarity in the maximum vapor-saturation pressures (~3 kbars) recorded in melt inclusions from a wide range of spreading rates reflects a relatively uniform CO_2 content of 50–85 ppm for the depleted upper mantle feeding the global mid-ocean ridge system.

1. Introduction

The oceanic crust is formed from solidification of magmas produced during decompression melting of upwelling mantle beneath mid-ocean ridges (MORs). The release of latent heat during cooling and crystallization drives hydrothermal circulation at the seafloor and influences geothermal gradients in the oceanic lithosphere [e.g., *Maclennan*, 2008]. Thus, crystallization at MORs is a primary mechanism by which heat and material are transferred from the Earth's interior to the crust, oceans, and atmosphere [e.g., *Lowell et al.*, 2008]. However, due to the inherent difficulty in observing these petrologic processes in situ, the depth and distribution of crystallization in the crust and mantle beneath MORs remains poorly constrained.

There are two end-member models for the distribution of crystallization beneath MORs: (1) focused accretion and (2) distributed accretion. Focused accretion is classically manifest in the gabbro glacier model [*Quick and Denlinger*, 1993], which supposes that melt is fed directly from the mantle to a shallow axial magma chamber [e.g., *Sleep*, 1975; *Nicolas et al.*, 1988; *Quick and Denlinger*, 1993; *Phipps Morgan and Chen*, 1993; *Henstock et al.*, 1993]. The lower crust is then created from subsidence or downward/outward flow of phenocrysts formed during crystallization in the axial magma chamber. In the gabbro-glacier model little to no crystallization occurs in the lower crust or upper mantle, though a variation on this model invokes two zones of focused accretion: a shallow zone in the middle to upper crust and a second zone at the base of the crust [e.g., *Chen*, 2001].

By contrast, models of distributed accretion are primarily based on observations from ophiolites that suggest crystallization occurs over a range of depths [*Boudier and Nicolas*, 1996; *Kelemen et al.*, 1997a, 1997b]. The archetypal example of distributed accretion is the multiple sills model, which advocates for in situ crystallization in a series of stacked sills spanning from the mantle to the seafloor [e.g., *Kelemen et al.*, 1997a, 1997b; *Korenaga and Kelemen*, 1997; *Kelemen and Aharonov*, 1998]. The depth of sill emplacement is controlled by the formation of permeability barriers in response to rapid crystallization of plagioclase and pyroxene during melt ascent [e.g., *Kelemen and Aharonov*, 1998]. A hybrid of this model takes into account

the petrologic stratification of the oceanic crust and allows for the upper crust to form directly from crystallization in the shallow melt lens, while the lower crust undergoes in situ crystallization during magma ascent [e.g., *Maclennan et al*., 2004]. Interestingly, neither of these end-member accretion models includes significant crystallization in the uppermost mantle, despite petrologic evidence that crystallization begins below the crust-mantle transition [e.g., *Tormey et al*., 1987; *Cannat et al*., 1992; *Grove et al*., 1992; *Elthon et al*., 1995; *Michael and Cornell*, 1998; *Kelemen et al*., 2007; *Collier and Kelemen*, 2010].

One approach to determining pressures of crystallization beneath actively accreting MORs is through major element thermobarometry [e.g., *Grove et al*., 1992; *Langmuir et al*., 1992; *Yang et al*., 1996; *Cannat et al*., 1997; *Michael and Cornell*, 1998; *Herzberg*, 2004; *Villiger et al*., 2007]. These major element barometers are based on calibrations from experiments that map the saturation surfaces of olivine, plagioclase, and clinopyroxene at variable pressures (from 1 to 16 kbar) in basaltic systems [e.g., *Tormey et al*., 1987; *Elthon et al*., 1995; *Grove et al*., 1992]. Crystallization pressures calculated using major element compositions from basalts erupted at different MORs show that crystallization occurs from the top of the melting regime to the seafloor [*Grove et al*., 1992; *Yang et al*., 1996; *Michael and Cornell*, 1998; *Herzberg*, 2004; *Villiger et al*., 2007]. Furthermore, pressures generally increase with decreasing spreading rate [e.g., *Grove et al*., 1992; *Michael and Cornell*, 1998; *Herzberg*, 2004], which is consistent with colder thermal conditions beneath slower-spreading ridges [e.g., *Reid and Jackson*, 1991; *Bown and White*, 1994; *White et al*., 2001]. A limitation of these barometers is that they require magmas to be multiply saturated with olivine + plagioclase + clinopyroxene, which is not the case for all MOR basalts. Furthermore, this approach produces a single pressure despite the fact that magmas likely experience various extents of polybaric crystallization during ascent through the mantle and crust.

An alternative approach to determining the distributions of crystallization beneath MORs is to use vapor-saturation pressures derived from volatile contents in melt inclusions [e.g., *Saal et al*., 2002; *Wanless and Shaw*, 2012]. Melt inclusions are droplets of melt that are trapped in crystallizing phenocrysts during ascent through the magmatic system. Vapor-saturation pressures of melt inclusions, which are derived from CO_2 and H_2O contents using experimental results of *Dixon and Stolper* [1995], provide an estimate of the pressure of melt entrapment or crystallization in MOR systems [e.g., *Saal et al*., 2002; *Wanless and Shaw*, 2012] and thus do not record a polybaric crystallization history. Vapor-saturation pressures of olivine-hosted melt inclusions from several MORs show that crystallization occurs over a wide range of pressures from the uppermost mantle to the seafloor [*Saal et al*., 2002; *Shaw et al*., 2010; *Wanless and Shaw*, 2012; *Wanless et al*., 2014; *Colman et al*., 2015, *Wanless et al*., 2015; *Le Voyer et al*., 2017].

In this study, we combine crystallization pressures calculated from major element contents (Major Element Pressures: MEPs) of basaltic glasses and vapor saturation pressures (VSPs) recorded in naturally glassy olivine-hosted melt inclusions and basaltic glasses to assess the distribution of crystallization along the global MOR system. We calculate crystallization pressures from >9000 basaltic glasses erupted along the global ridge system [*Gale et al*., 2013] using both major element barometers and fractional crystallization trends produced using petrologic models. We also calculate VSPs from 432 basaltic glasses (from PetDB) and >400 olivine-hosted melt inclusions from five MORs with spreading rates from 1to 11 cm/yr (full rate). We show that (1) both major element and vapor-saturation pressures increase with decreasing spreading rate, (2) crystallization occurs in the lower crust and upper mantle at all ridges, even when a melt lens is present, and (3) a significant amount of crystallization occurs at the base of a sloping lithosphere at all spreading rates, which can account for crystallization at pressures up to 6 kbar at the slowest spreading ridges. We use these results to produce a conceptual model for crustal accretion along the global MOR system. Finally, we suggest that the remarkably similar maximum VSPs recorded in melt inclusions across all spreading rates (~3 kbars) reflects a relatively uniform CO_2 content of 50–85 ppm for the depleted upper mantle feeding the global MOR system.

2. Basalt Crystallization Pressures

2.1. Major Element Pressure (MEP) Calculations

The composition of mid-ocean ridge basalts (MORB) reflects a variety of subsurface processes [e.g., *Sinton and Detrick*, 1992; *Perfit and Chadwick*, 1998; *Klein*, 2005; *White and Klein*, 2014]. In addition to fractional crystallization, reactive crystallization in dunite channels [e.g., *Kelemen et al*., 1995, 1997a, 1997b; *Collier and*

Kelemen, 2010; *Liang et al*., 2010], melt rock reactions in the lithosphere [e.g., *Drouin et al*., 2009; *Sanfilippo et al*., 2014; *Paquet et al*., 2016], or the gabbroic crust [e.g., *Lissenberg and Dick*, 2008; *MacLeod et al*., 2013], mantle source heterogeneity [e.g., *Sims et al*., 2002; *Donnelly et al*., 2004; *Shimizu et al*., 2016], variations in depths or extents of melting [e.g., *Klein and Langmuir*, 1987; *Langmuir et al*., 1992; *Perfit et al*., 1994], and crustal assimilation [e.g., *Michael and Schilling*, 1989; *Wanless et al*., 2010] can all modify trace element contents and, depending on the phases involved, alter the CaO, Al_2O_3, and MgO content of erupted basalts [e.g., *Michael and Shilling*, 1989; *Lissenberg and Dick*, 2008; *Paquet et al*., 2016]. For example, melt rock reaction in gabbroic rocks may involve the dissolution of olivine and crystallization of clinopyroxene [*Paquet et al*., 2016] changing the CaO/Al_2O_3 of the melt. However, despite the numerous processes acting on ascending melts, fractional crystallization plays a dominant role in controlling MORB major element contents [*Sinton and Detrick*, 1992; *Perfit and Chadwick*, 1998; *Rubin and Sinton*, 2007; *Klein*, 2005; *White and Klein*, 2014] and, therefore, erupted basalt compositions have been widely used to evaluate pressures of crystallization at MORs [*Grove et al*., 1992; *Yang et al*., 1996; *Cannat et al*., 1997; *Michael and Cornell*, 1998; *Herzberg*, 2004; *Villiger et al*., 2007].

Here we use a recent compilation of >9000 MOR basalts [*Gale et al*., 2013] to calculate pressures of crystallization along the global MOR system using (1) major element barometers and (2) petrologic modeling. The MEP of every basalt is calculated using the barometer of *Herzberg* [2004], which parameterizes the ol-cpx-plag saturation surface from anhydrous experiments on basalt onto the anorthite-diopside-enstatite ternary diagram (invariant points and cotectics are derived from experimental data and are described in *Herzberg and O'Hara* [1998] and *Herzberg* [2004]). In addition, we calculate the pressures of crystallization using the calcium barometer (uncertainty ±0.7 kbar) in *Michael and Cornell* [1998], which calculates pressures based on experimental data and models from *Grove et al*. [1992] and *Yang et al*. [1996]. These pressures indicate a minimum for the onset of crystallization and a maximum final pressure of crystallization [*Michael and Cornell*, 1998]. A requirement of both barometers is that magmas are cosaturated with olivine, plagioclase, and clinopyroxene [e.g., *Danyushevsky et al*., 1996; *Yang et al*., 1996; *Michael and Cornell*, 1998; *Herzberg*, 2004]. Lavas that only experienced olivine or olivine + plagioclase crystallization will produce erroneous pressures. Thus, to filter the data set to include only melts that are multiply saturated we follow the approach of *Herzberg* [2004]. Samples saturated with only olivine and/or plagioclase are identified by excess CaO using the equation $CaO_{excess} = CaO + 0.3MgO + 14.5$ and samples with $CaO_{excess} > 0$ are removed from the data set. A caveat to using this approach to identify excess CaO is that it assumes all lavas have similar parental magma compositions. Unfortunately, this assumption is unlikely to be true across the global ridge system, where different degree melts are generated over a range of spreading rates and mantle potential temperatures.

An alternative approach to using major element compositions to determine crystallization pressures is through petrologic modeling. In this approach, pressures of crystallization are determined by comparing a suite of basalt compositions to petrologic models of fractional crystallization calculated at a variety of pressures from different starting compositions [e.g., *Michael and Cornell*, 1998]. While this approach has been effective for individual suites of lavas, applying it to the global ridge system is difficult due to the overwhelming number of samples, possible starting compositions, and range of melting systematics typical at ridges of different spreading rates. To circumvent this problem, we break the global data set into individual ridge segments (defined by *Gale et al*. [2013]) and compare basalts erupted at each segment to a series of modeled fractional crystallization trends (Figure 1) produced using the equations described in *Yang et al*. [1996]. The fractional crystallization trends are calculated using 32 starting compositions produced by various extents of melting simulated at eight spreading rates (0.5, 1, 2, 3, 4, 6, 8, and 10 cm/yr) and four mantle potential temperatures (1300, 1350, 1400, and 1450°C). These primary melt compositions are taken from calculations by *Behn and Grove* [2015] assuming passive, decompression melting of a homogenous depleted mantle [*Workman and Hart*, 2005] and were found to be a good fit to the global MORB data array. Each primary melt composition is allowed to crystallize at pressures ranging from 1–6 kbar. For each segment in the global data set, we compare the basalt compositions to the fractional crystallization trends calculated for the corresponding spreading rate. The best-fit trend is determined using a least squares regression (Figure 1) to the Al_2O_3, CaO, and MgO contents. We use the pressure of the best-fit trend to assign the appropriate pressure of crystallization for each segment along the global ridge system. This approach produces a single pressure that reflects the range of basalt compositions erupted at a given segment; however,

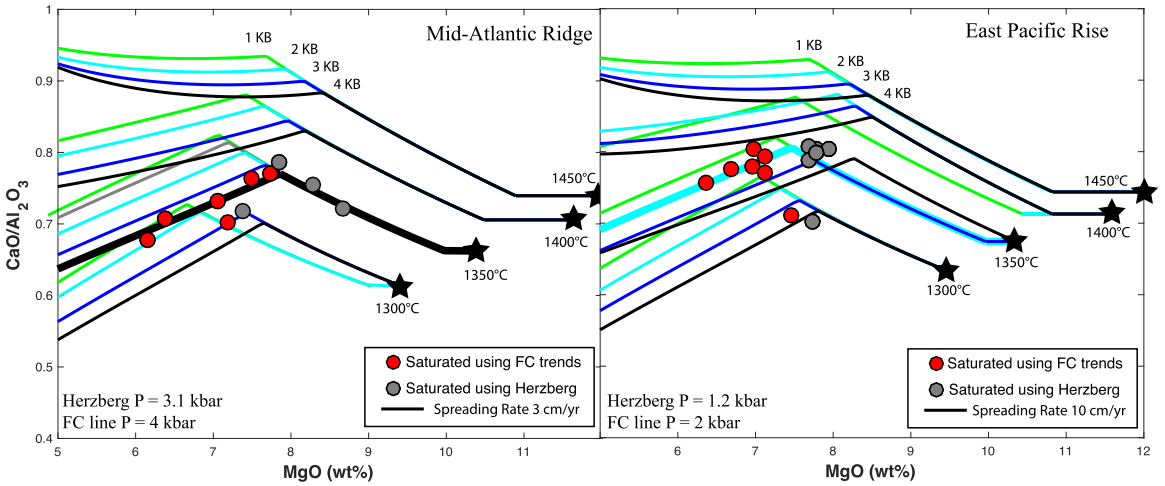

Figure 1. Example showing 16 of our 192 fractional crystallization trends used to determine crystallization pressures. Both the red and gray symbols represent the data from a single segment of the (a) MAR (segment #210) and (b) EPR (segment #20) that passed the Herzberg filter for three-phase saturation. While the red symbols are clearly multiply saturated based on the fractional crystallization trends (FC trends), the gray symbols may not have actually experienced clinopyroxene crystallization. Thus, the Herzberg equations may not accurately filter the data for multiply saturated lavas. The MEP using the Herzberg approach on segment 210 of the MAR yields a pressure of 3.1 kbar, while the best-fit FC line (thick black line) indicates a pressure of 4 kbar. On the EPR, the best-fit trend has a pressure of 2 kbar (thick light blue line), while the Herzberg barometer give pressures of 1.2 kbar. Fractional crystallization trends were produced using four mantle potential temperatures (black stars) and a single spreading rate, resulting in a wide range of starting compositions. Each starting composition was crystallized at various pressures (different colored lines) resulting in the 16 trends shown.

does not provide direct information on the polybaric distribution of crystallization beneath a MOR. A major benefit of this approach is that it eliminates the requirement of multiple phase saturation, which is difficult to verify in erupted MOR basalts, while simultaneously accounting for possible variations in mantle source composition.

2.2. Comparison of Major Element Barometer Pressure Calculations

The MEPs calculated using the *Herzberg* [2004] barometer are typically lower by 0.5–1.5 kbar compared to those calculated using the *Michael and Cornell* [1998]; however, estimates using both barometers result in the same trend with spreading rate (Figure 2 and supporting information Figure S1). Given the similarity in the trends inferred from both barometers we limit the remainder of our discussion to MEPs inferred from the *Herzberg* [2004] barometer and its comparison to the pressures inferred from petrologic modeling.

After applying the *Herzberg* CaO_{excess} filter to remove samples that are not multiply saturated, we are left with a data set that includes ~10,000 basalts. After further excluding plume-influenced segments defined in *Gale et al*. [2013], which have anomalously low crystallization pressures compared to typical ridge segments of similar spreading rates, as well as segments where there are fewer than 3 samples—the resulting global data set includes >9000 basalts from 195 segments. To facilitate comparison with the pressures inferred from the petrologic modeling, we focus on the average pressure calculated from all individual basalts for each segment. Note that the petrologic modeling approach allows us to assign a pressure only to those segments that have sufficient samples to generate a robust fit (i.e., R^2 values of >0.75).

2.3. Major Element Pressure Results

Using both the *Herzberg* barometer (Figure 2a) and the petrologic modeling approach (Figure 2b), average MEPs were calculated for each segment in the global data set. The pressures by segment were then averaged to produce a single pressure for each major mid-ocean ridge (Figures 2c and 2d). Using both approaches, there is a trend toward lower and less variable MEPs with increasing spreading rate when averaged by either segment or ridge (Figure 2). The *Herzberg* pressures are slightly deeper (~0.4 kbar) relative to the pressures inferred from petrologic modeling (Figure 2). One reason for this discrepancy may be that the CaO filtering does not accurately identify and exclude all 1 and two-phase saturated magmas from the *Herzberg* pressures. This is illustrated by the basalt compositions plotted in Figure 1, all of which have passed the CaO excess requirements of the *Herzberg* filter indicating that these lavas are predicted to be multiply saturated. Yet, when compared to the best-fit fractional crystallization trends (bold lines in Figure 1), it is clear many of these samples (gray data points in Figure 1) are not saturated with clinopyroxene and

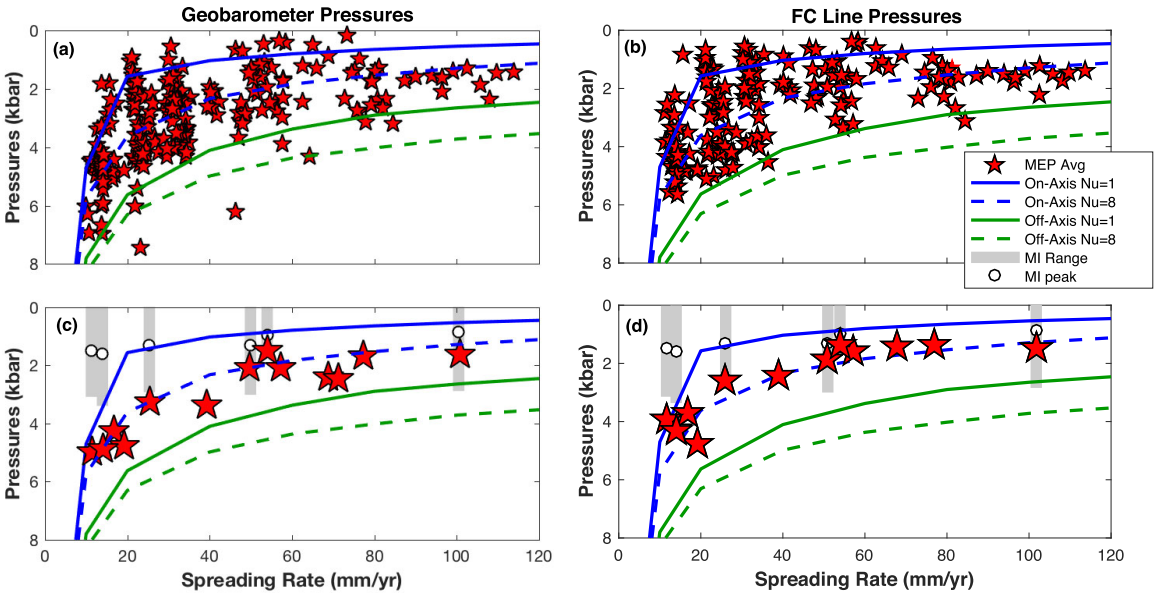

Figure 2. Major element pressures calculated for basaltic glasses and averaged by (a and b) spreading segment and (c and d) mid-ocean ridge versus spreading rate. Results in Figures 2a and 2c are pressures calculated using the major element barometers and results in Figures 2b and 2d are pressures calculated using our best fit fractional crystallization trend. Red stars in Figures 2a and 2b indicate pressures averaged from basalts erupted at 195 ridge segments and in Figures 2c and 2d indicate pressure averaged along 13 major ridges. White circles indicate the peak in melt inclusion VSPs at 5 ridges, while gray bars indicate the range of melt inclusion VSPs. Lines in both plots indicate the location of the 1150°C isotherm calculated at the ridge axis (blue) and 25 km off-axis (green) based on the thermal model of *Shaw and Lin* [1996]. The 1150°C isotherm corresponds to the minimum temperature where melts are multiply saturated [*Grove et al*., 1992]. Solid lines show the 1150°C isotherm calculated using a Nusselt number of 1 (no hydrothermal cooling), while the dashed lines use a Nusselt number of 8 (enhanced hydrothermal cooling).

therefore, some pressure estimates calculated using the *Herzberg* barometer are likely to be invalid. Detailed results of pressures calculated using the Herzberg barometer for each basalt, segment, and ridge are provided in supporting information Figures S4–S15; however, given the similarity in the trends inferred from both approaches, and the possibility that the Herzberg barometer may produce erroneous results, we limit the remainder of our discussion to results inferred from petrologic modeling (Figures 2b and 2d).

We investigated the depth distribution of crystallization by using the MEPs for each segment and plotting histograms of crystallization pressure as a function of spreading rate (Figures 3a–3d). A peak in the distribution of MEPs is observed at all spreading rates, with a shift to greater depths at slower spreading ridges (Figures 3a–3d). For example, fast (>80 mm/yr; full rate) and intermediate-spreading ridges (40–80 mm/yr) have shallow crystallization peaks at ∼1.5–1.6 kbars, while slow (20–40 mm/yr) and ultraslow-spreading ridges (<20 mm/yr) have peaks at ∼2.3 and ∼4.1 kbars, respectively. This shift in pressures is observed when the MEPs are binned by spreading rate (Figures 3a–3d) and by individual spreading ridge (see supporting information Figure S2). The decrease in MEPs with increasing spreading rate is consistent with previous studies on smaller MORB data sets [e.g., *Grove et al*., 1992; *Danyushevsky et al*., 1996; *Yang et al*., 1996; *Michael and Cornell*, 1998; *Herzberg*, 2004; *Villiger et al*., 2007]. This has been interpreted to indicate that thickening of the lithospheric lid causes the cessation of melting and onset of crystallization to occur deeper at slower-spreading ridges compared to faster-spreading ridges [e.g., *Grove et al*., 1992; *Bown and White*, 1994; *Michael and Cornell*, 1998].

2.4. Influence of Thermal Structure With Spreading Rate

Cooler thermal structures (and therefore, deeper isotherms) beneath slower-spreading ridges reflect a combination of slower upwelling rates, enhanced conductive cooling, and lower magma flux [*Sleep*, 1975]. While the temperature of three-phase saturation will vary with pressure, experimental studies and thermodynamic models suggest that basaltic magmas with MOR compositions should be multiply saturated with olivine, clinopyroxene, and plagioclase by 1150°C [*Grove and Bryan*, 1983]. Thus, we use the 1150°C isotherm to approximate the depth of multiple saturation. To estimate the depth of the 1150°C isotherm as a function of spreading rate we use the thermal model of *Shaw and Lin* [1996], which accounts for advective heat transport due to isoviscous mantle upwelling, the heat of magma injection, and the latent heat of

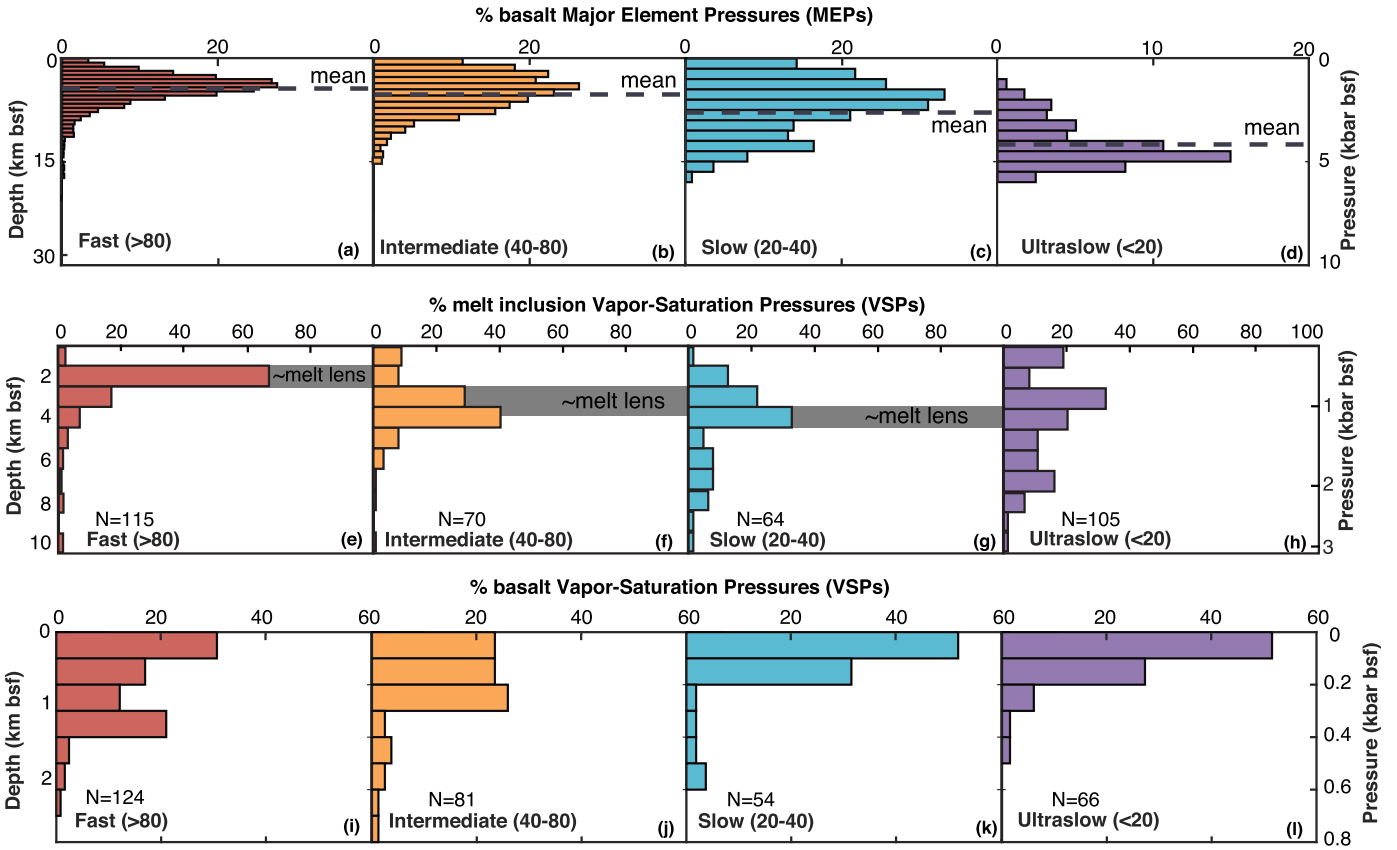

Figure 3. Histograms showing the percentage of crystallization at various pressures calculated from (a–d) MEPs in basaltic glasses, (e–h) VSPs of melt inclusions, and (i–l) VSPs of basaltic glasses at fast, intermediate, slow, and ultraslow spreading rates. Gray-dashed lines are the mean pressure and gray bars indicate the approximate pressure at the top of the seismically imaged melt lens.

crystallization in a narrow zone at the ridge axis. The effects of hydrothermal circulation are included using a Nusselt number approach [*Lin and Parmentier*, 1989], in which the thermal conductivity is increased by a factor above a specified cut-off depth (6 km) and at temperatures $<$600°C. This approach yields a variation in ridge thermal structure with spreading rate that is consistent with previous calculations [e.g., *Chen and Morgan*, 1990; *Phipps Morgan and Chen*, 1993].

We compare the resulting depth to the 1150°C isotherm calculated at the ridge axis to the MEPs assuming Nusselt numbers of 1 and 8 (solid and dashed blue curves in Figure 2, respectively). The calculated 1150°C isotherms predict the general trend of the data; however, even with efficient hydrothermal circulation (Nusselt number = 8), many of the MEPs from individual ridge segments extend to significantly greater pressures compared to the calculated three-phase saturation surface at all spreading rates. In the *Shaw and Lin* [1996] model formulation, greater Nusselt numbers cannot explain this discrepancy because the imposed cut-off depth for hydrothermal circulation, which is assumed to reflect the pressure at which cracks close and permeability decreases [*David et al*., 1994], suppresses hydrothermal heat extraction at depths $>$6 km.

One possible explanation for the deeper MEPs is that crystallization occurs below the lithosphere at higher temperatures within the melting regime [e.g., *Kelemen et al*., 1997a, 1997b]. Nearly simultaneous melting and crystallization in the mantle has been reconciled by models of diffusive chemical exchange between olivine and melt during porous mantle flow, when melt-rock ratios are low [e.g., *Kelemen et al*., 1997a, 1997b; *Collier and Kelemen*, 2010]. These models are supported by evidence of reactive crystallization in abyssal peridotites and in ophiolites [*Dick*, 1989; *Cannat et al*., 1992; *Niu*, 2004; *Kelemen et al*., 2007; *Collier and Kelemen*, 2010].

Alternatively, the difference between the calculated depth of the 1150°C isotherm beneath the ridge axis and the observed crystallization pressures may reflect pooling of off-axis melts over a region of finite width. Rising melts encounter a permeability barrier that can form due to rapid crystallization [*Sparks and*

Parmentier, 1991] and/or extensive melt rock reaction [e.g., *Drouin et al*., 2009] at the base of the lithosphere. The depth of this barrier will increase off-axis with a slope that is controlled by the spreading rate [*Hebert and Montési*, 2010]. This results in the formation of a decompaction channel in which melts accumulate off-axis and migrate upslope along the base of the lithosphere toward the ridge axis. The formation of such a channel requires rapid crystallization, and numerical modeling studies predict that significant volumes of melt are lost to crystallization into the lithospheric lid before the migrating melts reach the ridge axis [e.g., *Ghods and Arkani-Hamed*, 2000; *Katz and Weatherley*, 2012]. The major element chemistry of lavas erupted at the axis should reflect this protracted crystallization history and result in a range of MEPs, consistent with pressures at the base of the lithosphere.

One way to test if this model is consistent with the observed MEPs is to compare these pressures to the depth of the 1150°C isotherm calculated at a distance of 25 km from the ridge axis (Figure 2). This distance corresponds to width over which *Behn and Grove* [2015] found that melts are pooled to the ridge axis in order to explain the global variability in MORB major element chemistry, and is also consistent with trace element constraints on the width of melt pooling at the Gakkel ridge [*Wanless et al*., 2014]. In this scenario, the depth to the 1150°C isotherm at 25 km off-axis (green curves in Figure 2) should provide an upper bound on the observed MEPs, while the on-axis thermal structure (blue curves in Figure 2) represents the lower bound. Indeed, we find that the observed MEPs fall within the on and off-axis bounds for the 1150°C isotherm and are thus consistent with a model in which melts undergo crystallization as they migrate upslope along the base of the lithosphere toward the ridge axis. This implies that significant crystallization below the base of the lithosphere is not required to explain the range of MEPs observed along the global ridge system.

3. Vapor-Saturation Pressures (VSPs)

3.1. VSP Calculations

Vapor saturation pressures (VSPs) were calculated from CO_2 and H_2O contents of both basaltic glasses and melt inclusions using VolatileCalc [*Newman and Lowenstern*, 2002], which is calibrated on experimental results from *Dixon and Stolper* [1995] and *Dixon et al*. [1995]. These pressures are similar to pressures calculated using the parameterization of *Shishkina et al*. [2014] and within error of pressures calculated using Solex [*Witham et al*., 2012]. VSPs could not be calculated for the entire *Gale et al*. [2013] MORB data set because CO_2 contents are not consistently measured. Thus, we compiled basaltic glasses from PetDB for which reasonable CO_2 and H_2O contents were reported (N = 432) and used these data to calculate basalt VSPs.

For our melt inclusion data set, we take volatile contents of naturally glassy olivine-hosted melt inclusions (>400 samples) from studies of five MORs spanning fast to ultraslow-spreading rates [*Saal et al*., 2002; *Shaw et al*., 2010; *Wanless and Shaw*, 2012; *Wanless et al*., 2014, 2015; *Colman et al*., 2015]. Fast-spreading ridge melt inclusions are from two segments (9°50′N and 12°48′N) along the northern East Pacific Rise [*Wanless and Shaw*, 2012]. Intermediate-spreading rate melt inclusions are from two segments along the Juan de Fuca Ridge [Cleft and Vance segments; *Wanless and Shaw*, 2012] and two segments on the Galapagos Spreading Center [*Colman et al*., 2015]. Slow-spreading melt inclusions are from the Lucky Strike segment [*Wanless et al*., 2015], a magmatically robust section of the Mid-Atlantic Ridge. The ultraslow-spreading melt inclusions are from five volcanic centers along the Eastern Volcanic Zone of the Gakkel Ridge [*Wanless et al*., 2014]. Lucky Strike is one of two locations where a magma chamber has been imaged on a slow spreading center [*Singh et al*., 2006] and the Eastern Volcanic Zone is magmatically robust compared to the Sparsely Magmatic Zone of Gakkel Ridge [e.g., *Michael et al*., 2003]. Therefore, the melt inclusion VSPs from our slow and ultraslow sample suites reflect pressures of crystallization at magmatically robust segments; VSPs may vary at ridge segments with lower magma supply at these same spreading rates.

While this data set is smaller than the basaltic glasses used for MEPs, it spans the range of spreading rates at MORs and provides the first detailed comparison of melt inclusion pressures with MEPs along the global ridge system. We do not include data from off or near-axis seamounts, undersaturated melt inclusions, or plagioclase-hosted melt inclusions. A direct comparison of VSPs and MEPs from the same segments is provided in supporting information Table S1.

We account for the presence of vapor bubbles within the melt inclusions using mass balance, following the methods described by *Hauri et al*. [2002] and outlined in *Wanless and Shaw* [2012]. While this approach may not accurately reflect the actual CO_2 content in the vapor bubble, in *no instance* does the correction increase the pressure estimates beyond the estimates from inclusions without vapor bubbles from the same location. A comparison of pressures of crystallization for corrected and uncorrected melt inclusions is provided in supporting information Figure S16. We convert VSPs to pressures of crystallization b.s.f. by accounting for the pressure of the overlying water column based on the depth from which the host basalt sample was acquired [e.g., *le Roux et al*., 2006; *Wanless and Shaw*, 2012]. We note that these pressures are likely minimums, as the vapor bubbles may contain significantly more CO_2 then is accounted for in mass balance calculations [*Moore et al*., 2015], the inclusions may undergo reequilibration [e.g., *Gaetani et al*., 2012] during storage in the crust, or CO_2 may be lost during decrepitation if the inclusion undergoes a pressures change greater then ~2.5 kbar [*Maclennan*, 2017].

3.2. VSP Results

Volatile contents indicate that the basaltic glasses have vapor saturation pressures that range from supersaturated to undersaturated, with a majority in equilibrium with their eruption depths, while nearly all melt inclusions are supersaturated for their eruption depths (Figure 4a). Basaltic glasses have VSPs that range from their eruption pressure at or near the seafloor (consistent with equilibrium degassing during ascent) to ~1 kbar bsf (Figures 4a and 4b). By contrast, melt inclusions have VSPs that extend from the seafloor to the uppermost mantle (Figure 4c). The overall range of VSPs in melt inclusions is remarkably similar across all spreading rates, with maximum pressures up to ~3 kbars bsf (Figure 4c). We note that over 97% of our melt inclusions have entrapment pressures below the minimum threshold of decrepitation (2.5 kbar;

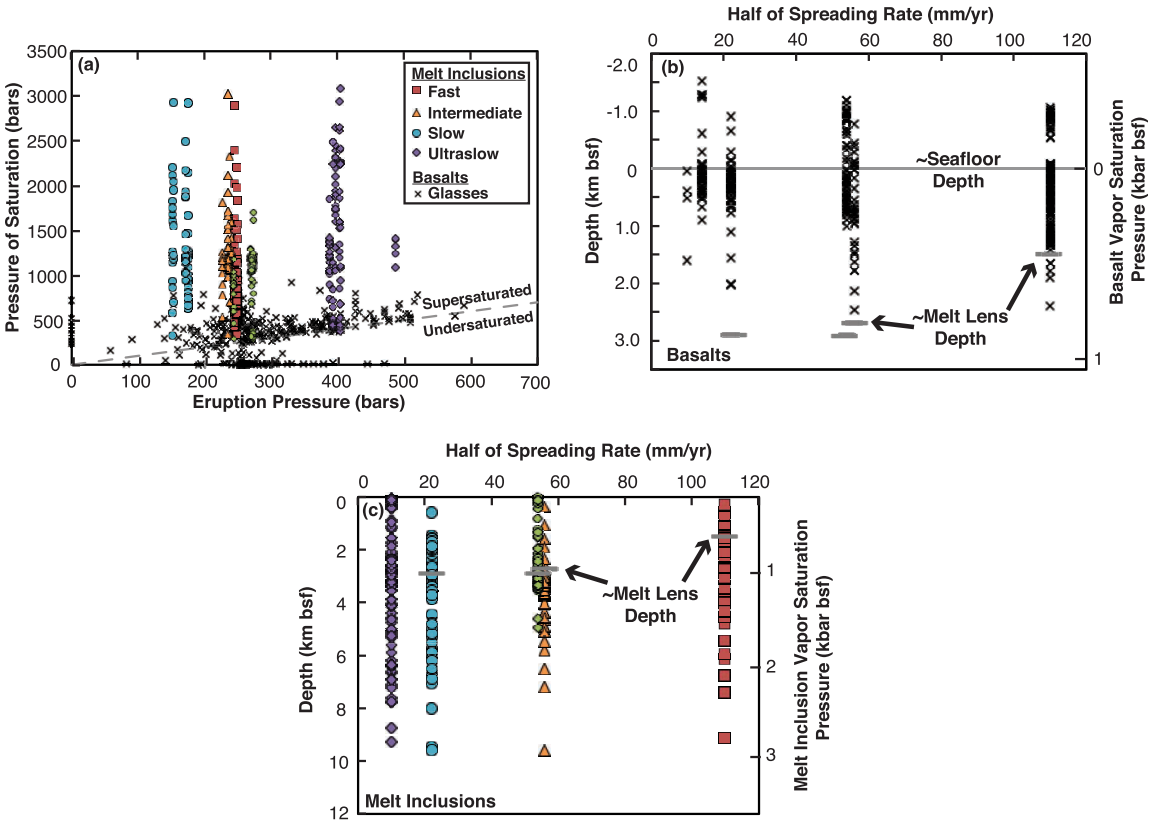

Figure 4. Comparison of pressures of crystallization based on volatile contents in basaltic glasses and melt inclusions. (a) Pressure of saturation (calculated from VolatileCalc) versus eruption pressure. Nearly all melt inclusions have pressures greater than or equal to the seafloor depths (supersaturated). By contrast, most (97%) basaltic glasses are undersaturated with respect to their eruption depth. (b) Basaltic glass vapor saturation versus spreading rate. Gray bar indicates the depth of the seafloor (equivalent to eruption depth for each sample). Basaltic glasses have pressures that range from the seafloor down to <1 kbar (below the seafloor; bsf). For ridges with a seismically imaged melt lens, almost all glasses have pressures less than the melt lens (short gray bars). (c) Vapor saturation pressures of melt inclusions versus spreading rate. Pressures range from the seafloor to approximately 3 kbar (bsf) at all spreading rates (note change in *y* axis scale compared to Figure 4b).

supporting information Figure S3) defined by *Maclennan* [2017]. Minimum melt inclusion VSPs vary slightly between ridges, but are generally greater than or equal to local seafloor depths.

Following the same procedures as for the MEPs, we examined the depth-distribution of crystallization as a function of spreading rate for the melt inclusion (Figures 3e–3h) and basalt (Figures 3i–3l) VSPs. Based on the basalt VSPs, there is a greater percentage of supersaturated basalts erupted at fast and intermediate-spreading ridges (Figures 3i, 3j, and 4b) compared to slower spreading ridges (Figures 3k, 3l, and 4b). Comparison of the melt inclusion distributions shows a deepening and defocusing of crystallization with decreasing spreading rate (Figures 3e–3h). In particular, there is a pronounced peak in VSPs in the shallow crust at fast-spreading ridges, which deepens and becomes less prominent at slower-spreading ridges (Figures 3e–3g). However, crystallization is not restricted to the shallow crust and extends into the lower crust and uppermost mantle at all spreading rates. At ultraslow-spreading ridges crystallization is relatively uniform as a function of depth (Figure 3h). The maximum melt inclusion VSPs are similar ($\sim$3 kbars) at all ridges (Figure 4c). These trends are also observed in the VSPs from the uncorrected melt inclusions (supporting information Figure S16).

3.3. Comparison of Melt Inclusion VSPs, the Axial Melt Lens, and Host-Olivine Mg#'s

We next compared the distribution of crystallization based on VSPs to the geophysical interpretations of crustal structure at MORs. Shallow axial magma chambers (or melt lenses) are nearly ubiquitous features on fast and intermediate-spreading ridges [*Detrick et al*., 1987; *Kent et al*., 1993; *Carbotte et al*., 2006; *Canales et al*., 2006; *Blacic et al*., 2008], but are observed infrequently at slow-spreading ridges [*Singh et al*., 2006]. Petrologic studies suggest that the seismically imaged melt lens at fast and intermediate-spreading centers is a region of significant melt storage and crystallization [e.g., *Sinton and Detrick*, 1992; *Rubin and Sinton*, 2007; *Rubin et al*., 2009] and end member gabbro glacier models of accretion suggest that all crystallization occurs within the melt lens [e.g., *Nicolas et al*., 1988; *Quick and Denlinger*, 1993; *Henstock et al*., 1993].

While melt inclusions studies from ocean island basalts have difficulty reconciling VSPs with geophysical constraints of crustal structure [e.g., *Maclennan*, 2017], results of our VSPs and seismic studies at MORs are remarkably consistent. We find that when present, the peaks in melt inclusion VSPs coincide with the depth of the seismically imaged melt lens (Figures 3e–3h). The melt lens at the fast-spreading EPR is located at $\sim$0.5 kbar [*Kent et al*., 1993], which correlates well with the peak in melt inclusions VSPs (Figure 3e). The melt inclusion VSP peak deepens to 0.7–1 kbar at intermediate-spreading centers (Figure 3f), consistent with the depth of the melt lens observed along the intermediate-spreading Juan de Fuca Ridge and Galapagos Spreading Center [*Carbotte et al*., 2006; *Canales et al*., 2006; *Blacic et al*., 2008]. A less prominent peak is found at the slow-spreading Lucky Strike segment of the Mid-Atlantic Ridge (Figure 3g). This peak correlates with the seismically imaged melt lenses ($\sim$1 kbar) observed at this magmatically robust segment [*Singh et al*., 2006], though the overall pattern of crystallization is more broadly distributed compared to faster-spreading ridges.

As spreading rate decreases, the peak in melt inclusion VSPs becomes less prevalent (Figure 3h). The relatively uniform distribution of VSPs at Gakkel Ridge suggests that there is no consistent depth of magma storage/crystallization in the oceanic crust ($<$3 kbar) at ultraslow-spreading ridges. Instead, accretion appears to occur uniformly from $\sim$3 kbar to the seafloor (Figure 3h). This is consistent with numerical models suggesting that magma chambers are unstable in the cold lithospheric conditions presumed at slower-spreading rates [*Phipps Morgan and Chen*, 1993]. Indeed, our thermal models predict that for spreading rates $<$10 mm/yr the 1150°C isotherm is located at pressures $>$5 kbar (Figure 2), well below the base of the crust. The absence of a prominent region of melt storage and crystallization is also consistent with extensive exposure of mantle peridotite at the seafloor [e.g., *Dick*, 1989; *Cannat*, 1993; *Cannat et al*., 1995; *Lagabrielle et al*., 1998] and geophysical results that indicate a near absence of a continuous gabbroic layer at ultraslow-spreading ridges [e.g., *Jokat and Schmidt-Aursch*, 2007; *Sleep and Warren*, 2014]. Thus, magmas at ultraslow-spreading ridges may ascend directly to the seafloor and erupt without significant crystallization at crustal depths or freeze quickly in the crust with little to no magmatic differentiation [e.g., *Rubin and Sinton*, 2007; *Wanless et al*., 2014]. Either way, crystallization at ultraslow-spreading rates appears to be distributed throughout the crust and uppermost mantle.

The systematic broadening of the crystallization distributions with decreasing spreading rate (Figures 3e–3h) may imply that the amount of crystallization occurring in the lower crust increases at slower spreading

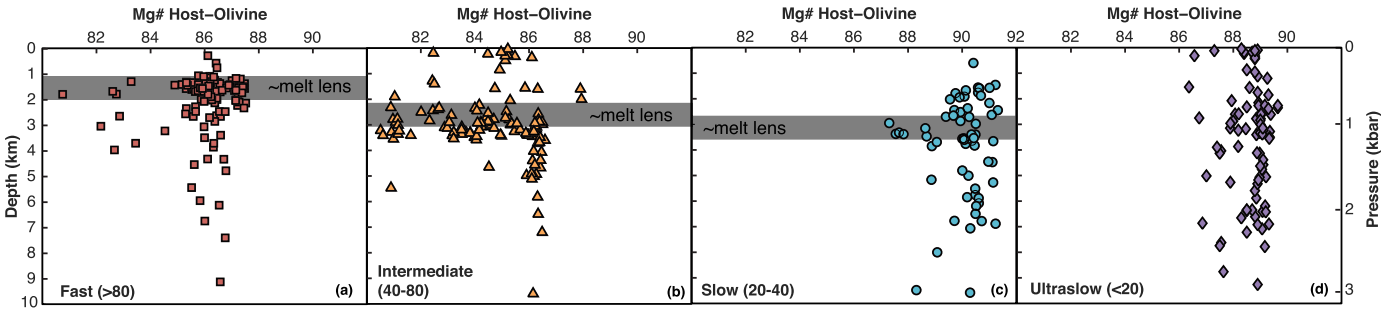

Figure 5. Mg# of host-olivine versus depth for four spreading rates: (a) fast, (b) intermediate, (c) slow, and (d) ultraslow. The highest variability in olivine Mg# occurs within the upper 4 km of the magmatic system. This generally correlates well with the depth of the melt lens, but suggests significant differentiation can occur below the melt lens, particularly at fast-spreading ridges. There is relatively limited variability at ultraslow-spreading ridges.

ridges. However, olivines (and melt inclusions) originally trapped at greater depths may reequilibrate during storage in the shallow melt lens [*Gaetani et al*., 2012; *Bucholz et al*., 2013], possibly skewing the distribution of crystallization at fast and intermediate-spreading rates towards the shallow crust. If so, the VSPs recorded at fast and intermediate-spreading ridges may underestimate the amount of crystallization occurring in the lower crust and uppermost mantle, further supporting models of distributed crustal accretion at MORs.

Recent studies from Iceland indicate that olivine-hosted melt inclusions can undergo significant decrepitation (or rupturing), where the CO_2 content of the inclusion is reset to be in equilibrium with the pressure at which decrepitation occurs [*Maclennan*, 2017]. Typically, decrepitation requires inclusions to undergo a relatively large pressure change ($\sim$2.5 kbar), and it is less likely to occur in melt inclusions formed at shallow pressures or in inclusions that undergo prolonged cooling histories. At MORs, the magmatic plumbing system is shallower than at ocean islands such as Iceland, and the majority of the melt inclusions are entrapped at pressures $<$2.5 kbar with a large fraction corresponding to the shallow melt lens (Figures 3e–3h). Moreover, prolonged storage and cooling in the warm oceanic crust and melt lens—as suggested by petrologic studies [e.g., *Sinton and Detrick*, 1992; *Rubin and Sinton*, 2007] and the wide range of Mg#s in the host-olivine (see below)—decrease the probability of decrepitation [*Maclennan*, 2017]. Thus, we argue it is unlikely that a majority of melt inclusions from MORs undergo significant decrepitation, and therefore that the measured CO_2 contents preserve the true pressure of melt entrapment.

The patterns of crystallization shown in Figures 3e–3h are consistent with the variability observed in the melt inclusion host-olivine Mg#s (Mg# = Mg/(Mg + Fe) *100), which is an indication of the extent of melt differentiation. Olivine in equilibrium with primitive mantle melts will have an Mg# near 90, while olivine crystallizing in more evolved magmas will have lower Mg#s. The large variability in the Mg# of host-olivines formed at, or near, the melt lens at fast and intermediate-spreading ridges (Mg# = 80 – 88) indicates significant magmatic differentiation occurs at these pressures (Figures 5a and 5b). By contrast, the Mg# of the host-olivines are higher and less variable (Mg# = 86 – 91) at slow and ultraslow-spreading ridges (Figures 5c and 5d), suggesting limited time in warm crustal reservoirs that promote crystallization and differentiation. This supports the hypothesis that magmas undergo prolonged storage in the warm shallow crust at fast and intermediate-spreading systems, where the melt lens is nearly steady state; but that magma ascends through the crust and lithosphere with little differentiation at slower spreading rates, where the thermal structure is much cooler [e.g., *Rubin and Sinton*, 2007; *O'Neill and Jenner*, 2012].

Traditional stacked sill models of accretion imply increasing extents of fractional crystallization with decreasing depth in the oceanic crust [e.g., *Kelemen et al*., 1998], which should be reflected in host-olivine Mg#'s. However, instead of a systematic decrease in Mg# with decreasing depth in the crust (implying increasing extents of crystallization), we observe increasing compositional variability (including both high and low Mg# olivine) with decreasing depth (Figure 5). This indicates that relatively primitive magmas can move from the base of the crust to the melt lens or seafloor with little to no differentiation, while other batches of magma undergo continuous crystallization throughout the crust. Taken together these observations suggest that melts ascend from the mantle to the melt lens through a variety of mechanisms. It is important to note that, with the exception of the Mid-Atlantic Ridge, the majority of the olivines are not in equilibrium with primitive mantle melts (Mg# $\geq$ 89). This supports the MEP data (Figure 2), which indicate crystallization

and therefore, magma differentiation, is occurring at the base of the lithosphere in the uppermost mantle, and thus, it is rare for a primary melt to reach crustal depths.

In summary, melt inclusion VSPs support the hypothesis that significant magma storage and crystallization is focused in the melt lens at fast and intermediate-spreading ridges [e.g., *Wanless and Shaw*, 2012], and also at magmatically robust slow-spreading ridge segments [*Wanless et al*., 2015]. However, the melt inclusion VSPs also indicate that crystallization occurs below the melt lens in the lower crust and mantle at all spreading rates (Figures 3e–3h), which is inconsistent with a pure gabbro glacier style of crustal accretion. These results indicate that, in this case, melt inclusions VSPs can record a shallower pressure of entrapment compared to some of the basalt MEPs. This may indicate that other processes (e.g., maxim CO_2 content of the mantle; ability to transport mantle olivine through the plumbing system, or host-olivine decrepitation) can limit the ability to use VSP to see deep into the melting region (see section 3.5).

3.4. Basaltic Glass VSPs

In contrast to VSPs from melt inclusions, basaltic glasses (Figure 4a) erupted at MORs generally have VSPs that are in equilibrium with the seafloor, though some are super-saturated with volatiles for their eruption pressures [e.g., *Dixon et al*., 1988; *Jambon et al*., 1995; *Simons et al*., 2002; *Wallace and Roberge*, 2004; *Cushman et al*., 2004; *Chadwick et al*., 2005; *le Roux et al*., 2006; *Standish et al*., 2008; *Soule et al*., 2012; *Wanless et al*., 2011; *Le Voyer et al*., 2015]. The eruption of supersaturated basalts is generally attributed to rapid ascent of magma from a shallow melt lens to the seafloor via diking [e.g., *Dixon et al*., 1988; *le Roux et al*., 2006]. Basalts erupted at fast and intermediate-spreading ridges have maximum VSPs that are consistent with equilibration within the seismically imaged melt lens at ~0.5–0.8 kbar (Figure 3). At the fast-spreading EPR, four glasses (out of 96) have pressures that extend up to 1 km below the top of the melt lens (Figure 4c); however, three of the four lie within 0.5 km of the top of the lens, which is within error of the pressure estimates. The one glass that has a pressure statistically below the top of the melt lens may have originated within a deeper portion of the melt lens, or the slightly higher pressure may reflect temporal changes in melt lens depths within the crust [e.g., *Detrick et al*., 1993; *Coogan et al*., 2003].

Maximum basalt VSPs from slow and ultraslow-spreading ridges are slightly shallower compared to fast and intermediate-spreading ridges (Figure 3). This may result from shallower storage depths, slower ascent rates that allow for volatile equilibration during ascent, and/or lower effusion rates due to lower magma flux that allows for greater extents of degassing during eruption. We favor lower effusion rates or slower ascent rates, as there is no evidence for shallow crustal magma chambers on ultraslow-spreading ridges, although a deeper, subcrustal magma chamber has been hypothesized at the Gakkel Ridge [*Shaw et al*., 2010].

3.5. Implications for the CO_2 Content of Mantle

As spreading rate varies along the global MOR system, there are significant changes in ridge axis morphology, bathymetry, lava compositions, and depths of crystallization; however, the maximum depth of crystallization based on melt inclusion VSPs is similar at all ridges examined (~3 kbars; Figure 4c). This suggests that the processes involved in producing and/or retaining volatile contents are independent of spreading rate and magma flux. Instead, the maximum melt inclusion VSPs could reflect (1) the maximum depth that olivine can crystallize beneath MORs, (2) the maximum depth over which olivine phenocrysts can be transported through the upper mantle/crust to erupt on the seafloor (i.e., there is a filter at ~3 kbar), (3) decrepitation or other processes that control the maximum CO_2 content of a melt inclusion, or (4) the maximum CO_2 content in a MOR melt.

The first hypothesis is inconsistent with the results of the crystallization pressures calculated using major element barometers, as shown in previous sections. Additionally, gabbros are observed in drill cores of the upper mantle [e.g., *Kelemen et al*., 2007], suggesting crystallization occurs well below the crust-mantle transition. Finally, experimental results indicate that olivine is stable at these pressures and is one of the first phases to crystallize [e.g., *Grove et al*., 1992]. Thus, we consider this hypothesis unlikely.

The second hypothesis cannot be ruled out; however, the differences in the shallow magmatic plumbing systems at ridges with different spreading rates (i.e., no melt lens at slower-spreading rates versus a steady-state melt lens at fast and intermediate-spreading ridges) suggests that olivine phenocrysts should be transported from different depths at different spreading rates—which is not observed. In section 3.3, we argued that decrepitation does not significantly affect the CO_2 contents in the majority of MOR melt inclusions;

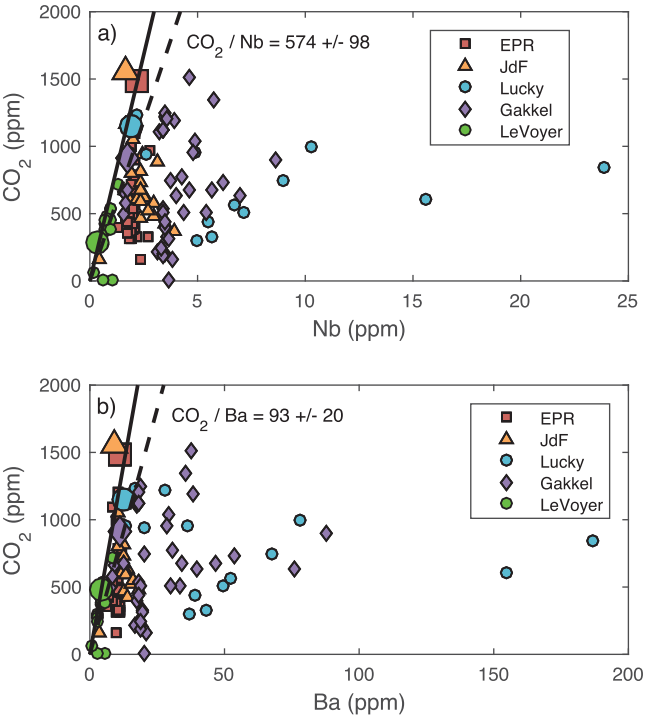

Figure 6. Melt inclusion CO2 versus (a) Nb and (b) Ba from four mid-ocean ridges. Small symbols indicate the composition of each melt inclusion analyzed, while large symbols are the melt inclusions with the maximum CO2 content at each ridge. The solid line represents a regression through the four highest CO2 content melt inclusions, while the dashed lines are a regression through the five highest CO2 contents at each ridge. CO2/Nb ratios and CO2/Ba ratios, which are calculated from the solid regression lines, are used to estimate the CO2 content of the depleted MORB mantle source. Green symbols are undersaturated melt inclusions from *Le Voyer et al*. [2017].

however, this process may influence inclusions entrapped at pressures greater than the decrepitation threshold of ~2.5 kbar, including the melt inclusions with the most enriched CO_2 contents (supporting information Figure S3). Recent studies of undersaturated glasses [*Michael and Graham*, 2015] and melt inclusions [*Le Voyer et al*., 2017] from MORs have used CO_2/Ba ratios in these inclusions to estimate the CO_2 content of the depleted upper mantle. As we discuss below, the CO_2 contents estimated using similar trace element ratios in our (saturated) melt inclusions are within error of these estimates. It would therefore be highly fortuitous if these MOR melt inclusions have undergone decrepitation and yet still yield the same mantle CO_2 estimates as the undersaturated melt inclusions and basalts. Therefore, we argue that the MOR melt inclusions have not undergone extensive decrepitation and instead, the maximum VSPs reflect the maximum CO_2 content of the depleted upper mantle.

If this hypothesis is correct, we can estimate the CO_2 content of the depleted mantle source for each ridge based on the maximum melt inclusion CO_2 contents and the concentration of trace elements with similar compatibilities to CO_2 [*Saal et al*., 2002; *Shaw et al*., 2010; *Wanless and Shaw*, 2012; *Wanless et al*., 2014, 2015; *Le Voyer et al*., 2017]. While earlier studies typically used CO_2/Nb ratios to infer the CO_2 content of the MORB mantle, more recent studies have suggested that CO_2 has a partition coefficient closer to that of Ba during mantle melting [*Rosenthal et al*., 2015; *Michael and Graham*, 2015]. Calculating the CO_2/Nb and CO_2/Ba ratios of the least degassed, depleted MORB (Nb $<$1.5 ppm) melt inclusions from each ridge (large symbols in Figure 6), we determine values for CO_2/Nb and CO_2/Ba of 574 $\pm$ 98 and 93 $\pm$ 20, respectively. These CO_2/Ba values are remarkably similar to values from undersaturated basaltic glasses (CO_2/Ba = 89) [*Michael and Graham*, 2015] and undersaturated melt inclusions (CO_2/Ba = 97) [*Le Voyer et al*., 2017], suggesting that these samples have undergone minimal degassing.

To convert these values into estimates of mantle CO_2, we multiply the ratios by estimates of the Nb and Ba content of the MORB mantle from *Workman and Hart* [2005]. This results in mantle CO_2 concentrations of 85 $\pm$ 15 and 52 $\pm$ 11 ppm based on Nb and Ba, respectively (Figure 6). These estimates are within error of those by *Rosenthal et al*. [2015], who calculated a CO_2 content for the depleted MORB mantle of 75 $\pm$ 25 ppm. We note that these values are a direct linear function of the assumed Nb and Ba content of the depleted MORB mantle; other studies estimated slightly higher mantle CO_2 values (~136 ppm and 137 ppm) based on a higher assumed Nb content of the MORB mantle [e.g., *Shaw et al*., 2010; *Le Voyer et al*., 2017].

Here, we have used the least degassed *depleted* melt inclusion compositions to evaluate the depleted MORB mantle volatile contents along the global ridge system. However, while maximum CO_2 contents of *depleted* MORB mantle may be relatively similar at all ridges, mantle trace element concentrations are known to vary with mantle source. For example, melt inclusions from Gakkel Ridge and Lucky Strike display variable trace element contents, with Nb up to 24 ppm and Ba $>$ 180 ppm. The elevated Nb and Ba contents

relative to CO_2 in these enriched samples may result from degassing of mantle melts with similar CO_2/Nb ratios or may indicate that coupling of mantle CO_2 with Nb and Ba is not as simple as has been previously suggested [*Le Voyer et al*., 2017]. If the assumption that the upper mantle volatile contents scale with trace element enrichments is correct [e.g., *Le Voyer et al*., 2017], then the enriched inclusions have either undergone significant degassing prior to entrapment or may have experience decrepitation during ascent from depth [*Maclennan*, 2017]. Intriguingly, undegassed MORB melt inclusions such as those from the Siqueiros fracture zone [*Saal et al*., 2002] show correlations between CO_2/Nb and CO_2 concentrations—indicating that use of a single ratio may not be a fully robust approach for estimating mantle CO_2 contents [*Helo et al*., 2011]. At Gakkel Ridge, the elevated Ba contents correlate with the presence of a metasomatized mantle component [e.g., *Michael et al*., 2003; *Wanless et al*., 2014] and such variability would translate directly into differences in the inferred mantle CO_2 content. Future studies are necessary to assess such source variability across the global mid-ocean ridge system.

4. Conceptual Model for Oceanic Crustal Accretion

The two approaches we use for estimating crystallization pressures (MEPs and VSPs) offer complementary perspectives on crustal accretion along the global MOR system. The MEPs provide constraints on average crystallization depths at a given segment, ridge, or spreading rate, but offer little insight into the fine-scale crystallization distributions within the crust. By contrast, VSPs offer a more detailed picture of crystallization in the crust and upper mantle, but are restricted to the uppermost 10 km due to the limitations imposed by the CO_2 content of the depleted upper mantle, constraints on the depths over which olivine phenocrysts can be transported through the magmatic plumbing system, and/or reequilibration of CO_2 contents due to melt storage and decrepitation. Combining the two approaches allows us to construct a conceptual model for crystallization beneath mid-ocean ridges as a function of spreading rate (Figure 7).

In our preferred model, melting in the mantle proceeds until upwelling ceases. Melts then ascend through the mantle until reaching the base of the lithosphere, which loosely corresponds to the depth at which temperature decreases sufficiently for crystallization to commence and a permeability barrier to form [*Sparks and Parmentier*, 1991]. To first order, the depth of this barrier is controlled by spreading rate, with shallower barriers corresponding to faster-spreading rates and higher magma flux [*Montési and Behn*, 2007; *Hebert and Montési*, 2010]. Both the peak and width of the depth distribution of MEPs (Figures 3a–3d) are consistent with melt migration and crystallization within a decompaction channel that extends ~25 km off-axis. Crystallization deeper in the mantle [e.g., *Kelemen et al*., 1997a, 1997b; *Collier and Kelemen*, 2010] or melt rock reaction [e.g., *Drouin et al*., 2009; *Sanfilippo et al*., 2014] may also contribute to the crystallization history. However, while these processes may occur simultaneously, crystallization along a sloping decompaction channel is consistent with our thermal calculations and the width of the melt pooling regime predicted by petrologic and numerical models of mantle melting and melt pooling [*Behn and Grove*, 2015]. In this scenario, crystallization in the mantle is controlled by the thickness and slope of the lithosphere away from the ridge axis, leading to a well-defined peak in the depth distribution of MEPs at all spreading rates.

By contrast, the pattern of crystallization in the crust differs between ridges of variable spreading rate. In our model, crystallization occurs from the base of the lithosphere to the seafloor at all spreading rates; however, there is prolonged storage and crystallization in the presence of a melt lens, which is consistent with previous petrologic models [e.g., *Sinton and Detrick*, 1992; *Rubin and Sinton*, 2007]. At fast and intermediate-spreading rates, melt storage, and crystallization in a shallow axial melt lens produces a prominent peak in VSPs. The lack of a steady-state melt lens at ultraslow-spreading ridges results in a more uniform distribution of crystallization as a function of depth in the upper 10 km (Figure 7), indicating that there is no preferred depth of melt storage within the lithosphere at ultraslow-spreading rates. This model is consistent with the relatively limited and more mafic host-olivine Mg#s (86–91) observed at slower spreading ridges. It also supports the absence of a steady-state melt lens in the cooler thermal regimes predicted by numerical models [e.g., *Phipps Morgan and Chen*, 1993] and likely reflects a more discontinuous crustal layer (where melts would repeatedly pool and crystallize) [e.g., *Cannat et al*., 1995; *Cannat*, 1996].

Finally, despite the prominent peaks in crystallization at fast and intermediate-spreading ridges, there is significant evidence for crystallization below the melt lens, indicating that magmas crystallize during ascent through the lower crust. Thus, the melt inclusion VSPs are inconsistent with purely top down gabbro glacier

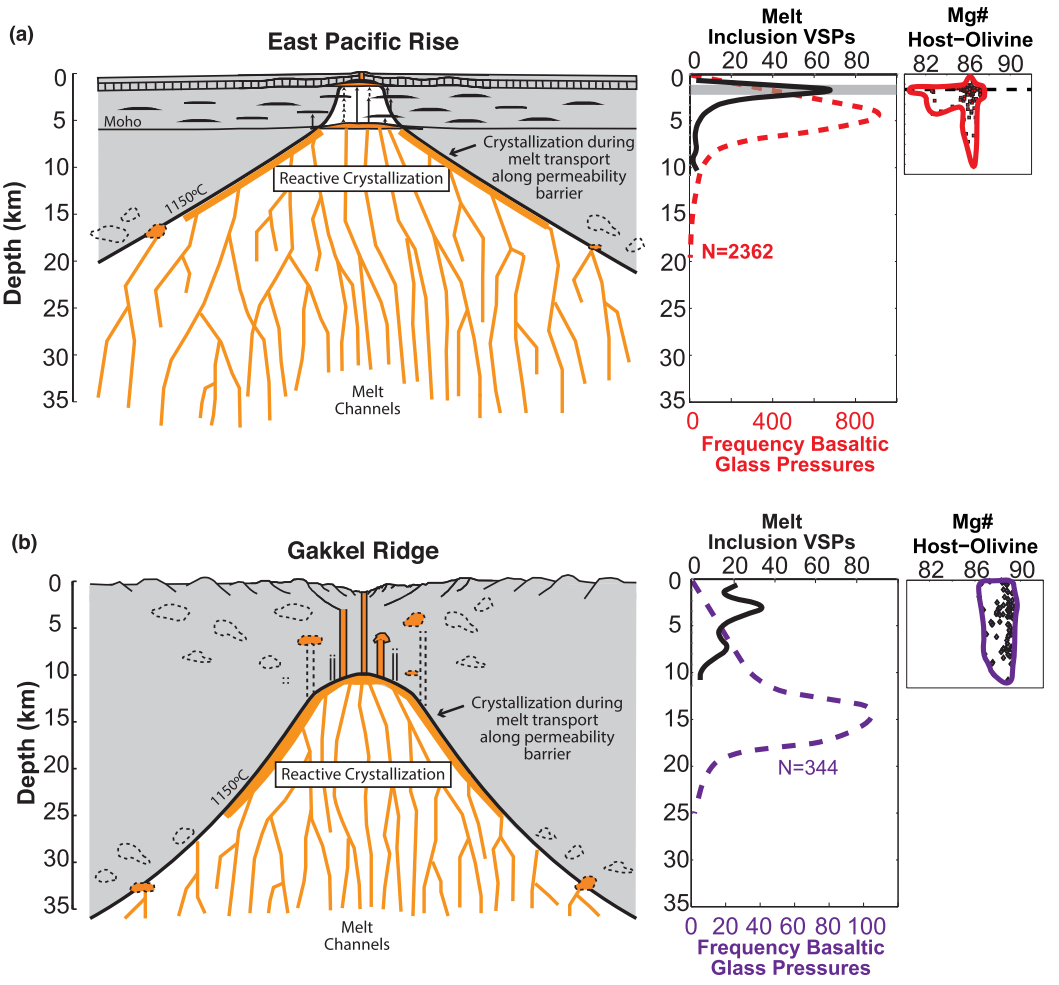

Figure 7. Cartoons of crustal accretion from two end member spreading rates: (a) fast-spreading and (b) ultraslow-spreading ridges based on the e different data sets (MEPs, VSPs, and Mg# of olivine) presented I this manuscript. (a) Fast-spreading ridges have VSPs and MEPs that occur within or near the crust, with peaks that correlate well with major geophysical transitions (MEPs = base of the crust; VSPs = melt lens). The peak in crystallization in the shallow crust recorded in the melt inclusions, suggests significant crystallization occurs within the melt lens, consistent with increased variability in host-livine Mg#'s. However, crystallization is not restricted to this depth and is distributed throughout the crust and mantle. There is a broad peak in MEPs that correlates with numerical models, indicating pooling and crystallization of magmas along a thickening lithosphere up to ~25 km off-axis. (b) Ultraslow-spreading ridges have a single peak in crystallization pressures that also correlates well with estimates for the base of the lithosphere. VSPs of melt inclusions indicate relatively uniform but limited crystallization in the upper 10 km, consistent with limited variability in host-olivine Mg#'s. However, there is a peak MEPs at ~5 km that extends to ~20 km, consistent with pooling of melts along the base of the lithosphere both on-axis and off-axis as calculated by our thermal mode.

models of crustal accretion [e.g., *Nicolas et al*., 1988; *Phipps Morgan and Chen*, 1993] and instead favor a model where accretion is distributed throughout the crust [e.g., *Kelemen et al*., 1997a, 1997b; *Kelemen and Aharonov*, 1998; *Wanless and Shaw*, 2012]. This interpretation is also consistent with the MEPs, which indicate average pressures below the melt lens at all depths. Further work is required to determine whether the decrease in VSPs corresponding to lower crustal and upper mantle pressures is a manifestation of the crystallization process itself or instead a reflection of the ability to transport olivine phenocrysts through the shallow magma plumbing system.

5. Conclusions

Here we present a conceptual model for crustal accretion along the global mid-ocean ridge system by combining pressures inferred from major element contents in >9000 basalts erupted at 195 ridge segments and vapor saturation pressures from melt inclusions from five ridges with a wide range of spreading rates. Estimates of crystallization pressures beneath mid-ocean ridges, including our new calculations from major

element and vapor saturation pressures indicate a shift in the depth of crystallization from fast to ultraslow-spreading systems (Figure 7). Major element pressures indicate that there is a peak in the depth of crystallization that deepens with spreading rate. The depth and width of this peak is consistent with a model in which melts are pooled and migrate from ~25 km off-axis toward the ridge axis within a decompaction channel that forms at the base of the sloping lithosphere, suggesting that this rheological boundary has a large influence on where magmas are stored and crystallize.

By contrast, vapor saturation pressures provide constraints on crystallization in the shallow magmatic system and show that crystallization occurs throughout the entire crust and uppermost mantle at all spreading rates—even in the presence of a melt lens. At faster-spreading rates, there are prominent peaks in crystallization that correlate well with the seismically imaged melt lenses. These peaks deepen and broaden with decreasing spreading rate. The vapor saturation peaks are consistent with the Mg#s of the host-olivine, indicating significant storage and crystallization occurs in the melt lens. At ultraslow-spreading rates, vapor saturation pressures become uniformly distributed and Mg#s of host olivine are higher, indicating that there is no preferred depth of melt storage and crystallization in the cold lithospheric crust.

Despite the systematic variability storage and crystallization observed with spreading rate, the maximum vapor saturation pressures are similar at all ridges (~3 kbar). This suggests that the mechanism responsible for these maximum pressures is independent of magma flux and thermal structure. Instead, we suggest that the maximum vapor saturation pressures reflect the CO_2 content of the depleted upper mantle feeding the global MOR system and imply a relatively constant mantle CO_2 content between 50–85 ppm for the depleted MORB mantle.

Acknowledgements
We thank G. Toltin for his assistance in melt inclusion sample preparation, B. Montelloni and the NENIMF facility at WHOI and N. Chatterjee for their assistance with data collection and Alison Shaw for conversations that motivated this study. We thank C. Langmuir for his thoughtful reviews and discussions, which greatly contributed to this manuscript. We also thank J. Maclennan and two anonymous reviewers for their insightful comments and J. Blichert-Toft. Data presented in this manuscript are available in the original citations or PetDB. This work was supported by the National Science Foundation [grant OCE-RIG-1524247 to V.D.W. and OCE-1458201 to M.D.B.] and the Sloan Foundation Deep Carbon Observatory.

References

Behn, M. D., and T. L. Grove (2015), Melting systematics in mid-ocean ridge basalts: Application of a plagioclase-spinel melting model to global variations in major element chemistry and crustal thickness, *J. Geophys. Res. Solid Earth*, *120*, 4863–4886, doi:10.1002/2015JB011885.

Blacic, T., G. Ito, A. Shah, and J. Canales (2008), Axial high topography and partial melt in the crust and mantle beneath the western Galapagos Spreading Center, *Geochem. Geophys. Geosyst.*, *9*, Q12005, doi:10.1029/2008GC002100.

Boudier, F., and A. Nicolas (1996), Magma chambers in the Oman ophiolite: Fed from the top and the bottom, *Earth Planet. Sci. Lett.*, *144*, 239–250.

Bown, J. W., and R. White (1994), Variation with spreading rate of oceanic crustal thicknesses and geochemistry, *Earth Planet. Sci. Lett.*, *121*, 435–449.

Bucholz, C. E., G. A. Gaetani, and M. D. Behn (2013), Post-entrapment modification of volatiles and oxygen fugacity in olivine-hosted melt inclusions, *Earth Planet. Sci. Lett.*, *374*, 145–155.

Canales, J. P., S. C. Singh, R. S. Detrick, S. M. Carbotte, A. Harding, G. M. Kent, J. B. Diebold, J. Babcock, and M. R. Nedimovic (2006), Seismic evidence for variations in axial magma chamber properties along the southern Juan de Fuca Ridge, *Earth Planet. Sci. Lett.*, *246*, 353–366.

Cannat, M. (1993), Emplacement of mantle rocks in the seafloor at mid-ocean ridges, *J. Geophys. Res.*, *98*, 4163–4172, doi:10.1029/92JB02221.

Cannat, M. (1996), How thick is the magmatic crust at slow spreading oceanic ridges?, *J. Geophys. Res.*, *101*, 2847–2857, doi:10.1029/95JB03116.

Cannat, M., D. Bideau, and H. Bougault (1992), Serpentinized peridotites and gabbros in the Mid-Atlantic Ridge axial valley at 15°37′N and 16°52′N, *Earth Planet. Sci. Lett.*, *109*, 87–106, doi:10.1016/0012-821X(92)90076-8.

Cannat, M., C. Mével, M. Maia, C. Deplus, C. Durand, P. Gente, P. Agrinier, A. Belarouchi, G. Dubuisson, and E. Humler (1995), Thin crust, ultramafic exposures, and rugged faulting patterns at the Mid-Atlantic Ridge (22–24 N), *Geology*, *23*, 49–52, doi:10.1130/0091-7613(1995)023<0049.

Cannat, M., F. Chatin, H. Witechurch, and G. Ceuleneer (1997), Gabbroic rocks trapped in the upper mantle at the Mid-Atlantic Ridge, *Proc. Ocean Drill. Program Sci. Results*, *153*, 243–264.

Carbotte, S., R. Detrick, A. Harding, J. Canales, J. Babcock, G. Kent, E. Van Ark, M. Nedimovic, and J. Diebold (2006), Rift topography linked to magmatism at the intermediate spreading Juan de Fuca Ridge, *Geology*, *34*, 209–212.

Chadwick, J., M. Perfit, I. Ridley, I. Jonasson, G. Kamenov, W. Chadwick, R. Embley, P. le Roux, and M. Smith (2005), Magmatic effects of the Cobb hot spot on the Juan de Fuca Ridge, *J. Geophys. Res.*, *110*, B03101, doi:10.1029/2003JB002767.

Chen, Y. (2001), Thermal effects of gabbro accretion from a deeper second melt lens at the fast spreading East Pacific Rise, *J. Geophys. Res.*, *106*, 8581–8588.

Chen, Y., and W. J. Morgan (1990), Rift valley/no rift valley transition at mid-ocean ridges, *J. Geophys Res.*, *95*, 17,583–17,604.

Collier, M. L., and P. B. Kelemen (2010), The case for reactive crystallization at mid-ocean ridges, *J. Petrol.*, *51*, 1913–1940, doi:10.1093/petrology/egq043.

Colman, A., J. M. Sinton, and V. D. Wanless (2015), Constraints from melt inclusions on depths of magma residence at intermediate magma supply along the Galapagos Spreading Center, *Earth Planet. Sci. Lett.*, *412*, 122–131, doi:10.1016/j.epsl.2014.12.007

Coogan, L., N. Mitchell, and M. O'Hara (2003), Roof assimilation at fast spreading ridges: An investigation combining geophysical, geochemical, and field evidence, *J. Geophys. Res.*, *108*(B1), 2002, doi:10.1029/2001JB001171.

Cushman, B., J. Sinton, G. Ito, and J. Dixon (2004), Glass compositions, plume-ridge interaction, and hydrous melting along the Galápagos Spreading Center, 90.5°W to 98°W, *Geochem. Geophys. Geosyst.*, *5*, Q08E17, doi:10.1029/2004GC000709.

Danyushevskyl, L. V., A. V. Sobolevz, and L. V. Dmitrievz (1996), Estimation of the pressure of crystallization and H2O content of MORB and BABB glasses: Calibration of an empirical technique, *Mineral. Petrol.*, *57*, 185–204.

David, C., T. F. Wong, W. Zhu, and J. Zhang (1994), Laboratory measurement of compaction-induced permeability change in porous rocks: Implications for the generation and maintenance of pore pressure excess in the crust, *Pure Appl. Geophys.*, *143*, 425–456.

Detrick, R. S., P. Buhl, E. Vera, J. Mutter, J. Orcutt, J. Madsen, and T. Brocher (1987), Multi-channel seismic imaging of a crustal magma chamber along the East Pacific Rise, *Nature*, *326*, 35–41, doi:10.1038/326035a0.

Detrick, R. S., A. J. Harding, G. M. Kent, J. A. Orcutt, J. C. Mutter, and P. Buhl (1993), Seismic structure of the southern East Pacific Rise, *Science*, *259*, 499–503, doi:10.1126/science.259.5094.499.

Dick, H. J. B. (1989), Abyssal peridotites, very slow spreading ridges and ocean ridge magmatism, *Geol. Soc. London Spec. Publ.*, *42*, 71–105, doi:10.1144/GSL.SP.1989.042.01.06.

Dixon, J. E., and E. M. Stolper (1995), An experimental study of water and carbon dioxide solubilities in mid-ocean ridge basaltic liquids. Part II: Applications to degassing, *J. Petrol.*, *36*, 1633–1646.

Dixon, J. E., E. Stolper, and J. R. Delaney (1988), Infrared spectroscopic measurements of CO2 and H2O in Juan de Fuca Ridge basaltic glasses, *Earth Planet. Sci. Lett.*, *90*, 87–104.

Dixon, J. E., E. M. Stolper, and J. R. Holloway (1995), An experimental study of water and carbon dioxide solubilities in mid-ocean ridge basaltic liquids. Part I: Calibration and solubility models, *J. Petrol.*, *36*, 1607–1631.

Donnelly, K., S. Goldstein, C. Langmuir, and M. Spiegelman (2004), Origin of enriched ocean ridge basalts and implications for mantle dynamics, *Earth Planet. Sci. Lett.*, *226*, 347–366.

Drouin, M., M. Godard, B. Ildefonse, O. Bruguier, and C. J. Garrido (2009), Geochemical and petrographic evidence for magmatic impregnation in the oceanic lithosphere at Atlantis Massif, *Chem. Geol.*, *264*, 71–88, doi:10.1016/j.chemgeo.2009.02.013.

Elthon, D., D. K. Ross, and J. K. Meen (1995), Compositional variations of basaltic glasses from the Mid-Cayman Rise spreading center, *J. Geophys. Res.*, *100*, 12,497–12,512, doi:10.1029/94JB02777.

Gaetani, G. A., J. A. O'Leary, N. Shimizu, C. E. Bucholz, and M. Newville (2012), Rapid reequilibration of H2O and oxygen fugacity in olivine-hosted melt inclusions, *Geology*, *40*, 915–918, doi:10.1130/G32992.1.

Gale, A., C. A. Dalton, C. H. Langmuir, Y. Su, and J.-G. Schilling (2013), The mean composition of ocean ridge basalts, *Geochem. Geophys. Geosyst.*, *14*, 489–518, doi:10.1029/2012GC004334.

Ghods, A., and J. Arkani-Hamed (2000), Melt migration beneath mid-ocean ridges, *Geophys. J. Int.*, *140*, 687–697.

Grove, T., and W. Bryan (1983), Fractionation of pyroxene-phyric MORB at low pressure: An experimental study, *Contrib. Mineral. Petrol.*, *84*, 293–309.

Grove, T. L., R. J. Kinzler, and W. B. Bryan (1992), Fractionation of mid-ocean ridge basalt (MORB), in *Mantle Flow and Melt Generation at Mid-Ocean Ridges*, Geophys. Monogr. Ser., vol. 71, edited by J. P. Morgan, D. K. Blackman, and J. M. Sinton, pp. 281–310, AGU, Washington, D. C.

Hauri, E., J. Wang, J. Dixon, P. King, C. Mandeville, and S. Newman (2002), SIMS analysis of volatiles in silicate glasses: 1. Calibration, matrix effects and comparisons with FTIR, *Chem. Geol.*, *183*, 99–114.

Hebert, L. B., and L. G. J. Montési (2010), Generation of permeability barriers during melt extraction at mid-ocean ridges, *Geochem. Geophys. Geosyst.*, *11*, Q12008, doi:10.1029/2010GC003270.

Helo, C., M.-A. Longpré, N. Shimizu, D. A. Clague, and J. Stix (2011), Explosive eruptions at mid-ocean ridges driven by CO_2-rich magmas, *Nat. Geosci.*, *4*, 260–263, doi:10.1038/ngeo1104.

Henstock, T., A. Woods, and R. White (1993), The accretion of oceanic crust by episodic sill intrusion, *J. Geophys. Res.*, *98*, 4143–4161.

Herzberg, C., (2004), Partial crystallization of mid-ocean ridge basalts in the crust and mantle, *J Petrol.*, *45*, 2389–2405, doi:10.1093/petrology/egh040.

Herzberg, C., and M. O'Hara (1998), Phase equilibrium constraints on the origin of basalts, picrites, and komatiites, *Earth Sci. Rev.*, *44*, 39–79.

Jambon, A., B. Déruelle, G. Dreibus, and F. Pineau (1995), Chlorine and bromine abundance in MORB: The contrasting behaviour of the Mid-Atlantic Ridge and East Pacific Rise and implications for chlorine geodynamic cycle, *Chem. Geol.*, *126*, 101–117.

Jokat, W., and M. C. Schmidt-Aursch (2007), Geophysical characteristics of the ultraslow spreading Gakkel Ridge, Arctic Ocean, *Geophys. J. Int.*, *168*, 983–998.

Katz, R. F., and S. M. Weatherley (2012), Consequences of mantle heterogeneity for melt extraction at mid-ocean ridges, *Earth Planet. Sci. Lett.*, *335–336*, 226–237, doi:10.1016/j.epsl.2012.04.042.

Kelemen, P. B., and E. Aharonov (1998), Periodic formation of magma fractures and generation of layered gabbros in the lower crust beneath oceanic spreading ridges, Faulting and magmatism at mid-ocean ridges, in *Faulting and Magmatism at Mid-Ocean Ridges*, vol. 106, edited by W. Roger Buck et al., pp. 267–289, AGU, Washington, D. C., doi:10.1029/GM106p0267.

Kelemen, P. B., N. Shimizu, and V. J. M. Salters (1995), Extraction of mid-ocean-ridge basalt from the upwelling mantle by focused flow of melt in dunite channels, *Nature*, *375*, 747–753, doi:10.1038/375747a0.

Kelemen, P. B., G. Hirth, N. Shimizu, M. Spiegelman, and H. Dick (1997a), A review of melt migration processes in the adiabatically upwelling mantle beneath oceanic spreading ridges, *Philos. Trans. Math. Phys. Eng. Sci.*, *355*, 283–318.

Kelemen, P. B., K. Koga, and N. Shimizu (1997b), Geochemistry of gabbro sills in the crust-mantle transition zone of the Oman ophiolite: Implications for the origin of the oceanic lower crust, *Earth Planet. Sci. Lett.*, *146*, 475–488.

Kelemen, P. B., E. Kikawa, D. J. Miller, and Shipboard Scientific Party (2007), Leg 209 summary: processes in a 20- km-thick conductive boundary layer beneath the Mid-Atlantic Ridge, 14°–16°N, edited by P. B. Kelemen, E. Kikawa, and D. J. Miller, *Proc. ODP, Sci. Results, 209*, Ocean Drill. Program, pp. 1–33, College Station, Tex., doi:10.2973/odp.proc.sr.209.001.2007.

Kent, G., A. Harding, and J. Orcutt (1993), Distribution of magma beneath the East Pacific Rise between the Clipperton transform and the 9 17′ N Deval from forward modeling of common depth point data, *J. Geophys. Res.*, *98*, 13,945–13,969.

Klein, E. M. (2005), Geochemistry of the igneous oceanic crust, in *The Crust: Treatise On Geochemistry*, vol. 3, edited by R. L. Rudnick, pp. 433–464, Elsevier, Pergamon, Oxford, U. K.

Klein, E. M., and C. H. Langmuir (1987), Global correlations of ocean ridge basalt chemistry with axial depth and crustal thickness, *J. Geophys. Res.*, *92*, 8089–8115.

Korenaga, J., and P. Kelemen (1997), Origin of gabbro sills in the Moho transition zone of the Oman ophiolite: Implications for magma transport in the oceanic lower crust, *J. Geophys. Res.*, *102*, 27,729–27,749.

Lagabrielle, Y., D. Bideau, M. Cannat, J. A. Karson, and C. Mével (1998), Ultramafic-mafic plutonic rock suites exposed along the mid-Atlantic ridge (10°N-30°N). Symmetrical-asymmetrical distribution and implications for seafloor spreading processes, in *Faulting and Magmatism at Mid-Ocean Ridges, Geophys. Monogr. Ser.*, vol. 106, edited by W. R. Buck et al., pp. 153–176, AGU, Washington, D. C., doi:10.1029/GM106p0153.

Langmuir, C., E. Klein, and T. Plank (1992), Petrological systematics of mid-ocean ridge basalts: Constraints on melt generation beneath ocean ridges, in *Mantle Flow and Melt Generation at Mid-Ocean Ridges, Geophys. Monogr. Ser.*, vol. 71, edited by P. Morgan, D. K. Blackman, and J. M. Sinton, pp. 183–280, AGU, Washington, D. C.

Le Roux, P., S. Shirey, E. Hauri, M. Perfit, and J. Bender (2006), The effects of variable sources, processes and contaminants on the composition of northern EPR MORB (8–10° N and 12–14° N): Evidence from volatiles (H2O, CO2, S) and halogens (F, Cl), *Earth Planet. Sci. Lett.*, *251*, 209–231.

Le Voyer, M., E. Cottrell, and K. A. Kelley (2015), The effect of primary versus secondary processes on the volatile content of MORB glasses: An example from the equatorial Mid-Atlantic Ridge (5° N–3° S), *J. Geophys. Res. Solid Earth*, *120*, 125–144, doi:10.1002/2014JB011160.

Le Voyer, M., K. A. Kelley, E. Cottrell, and E. H. Hauri (2017), Heterogeneity in mantle carbon content from CO2-undersaturated basalts, *Nat. Commun.*, *8*, 1–0, doi:10.1038/ncomms14062.

Liang, Y., A. Schiemenz, M. A. Hesse, E. M. Parmentier, and J. S. Hesthaven (2010), High-porosity channels for melt migration in the mantle: Top is the dunite and bottom is the harzburgite and lherzolite, *Geophys. Res. Lett.*, *37*, L15306, doi:10.1029/2010GL044162.

Lin, J., and E. M. Parmentier, (1989), Mechanisms of lithospheric extension at mid-ocean ridges, *Geophys. J. Int.*, *96*, 1–22, doi:10.1111/j.1365-246X.1989.tb05246.x.

Lissenberg, C., and H. Dick (2008), Melt-rock reaction in the lower oceanic crust and its implications for the genesis of mid-ocean ridge basalt, *Earth Planet. Sci. Lett.*, *271*, 311–325.

Lowell, R., J. Seewald, and A. Metaxas (2008), Modeling hydrothermal processes at ocean spreading centers, in *Magma to Microbe, Geophys. Monogr. Ser.*, vol. 178, edited by R. P. Lowell et al., pp. 1–14, AGU, Washington, D. C.

Maclennan, J. (2008), The supply of heat to mid-ocean ridges by crystallization and cooling of mantle melts, in *Magma to Microbe, Geophys. Monogr. Ser.* vol. 178, edited by R. P. Lowell, pp. 45–73, AGU, Washington, D. C., doi:10.1029/178GM04.

Maclennan, J. (2017), Bubble formation and decrepitation control the CO_2 content of olivine-hosted melt inclusions, *Geochem. Geophys. Geosyst.*, *18*, 597–616, doi:10.1002/2016GC006633.

Maclennan, J., T. Hulme, and H. Singh (2004), Thermal models of oceanic crustal accretion: Linking geophysical, geological and petrological observations, *Geochem. Geophys. Geosyst.*, *5*, Q02F25, doi:10.1029/2003GC000605.

MacLeod, C. J., C. Johan Lissenberg, and L. E. Bibby (2013), "Moist MORB" axial magmatism in the Oman ophiolite: The evidence against a mid-ocean ridge origin, *Geology*, *41*, 459–462, doi:10.1130/G33904.1.

Michael, P. J., and J.-G. Schilling (1989), Chlorine in mid-ocean ridge magmas: Evidence for assimilation of seawater-influenced components, *Geochim. Cosmochim. Acta*, *53*, 3131–3143.

Michael, P. J., and W. C. Cornell (1998), Influence of spreading rate and magma supply on crystallization and assimilation beneath mid-ocean ridges: Evidence from chlorine and major element chemistry of mid-ocean ridge basalts, *J. Geophys. Res.*, *103*, 18,325–18,356.

Michael, P. J., and D. W. Graham (2015), The behavior and concentration of CO2 in the suboceanic mantle: Inferences from undegassed ocean ridge and ocean island basalts, *Lithos*, *236–237*, 338–351, doi:10.1016/j.lithos.2015.08.020.

Michael, P. J., et al. (2003), Magmatic and amagmatic seafloor generation at the ultraslow-spreading Gakkel ridge, Arctic Ocean, *Nature*, *423*, 956–961, doi:10.1038/nature01704.

Montési, L. G., and M. D. Behn (2007), Mantle flow and melting underneath oblique and ultraslow mid-ocean ridges, *Geophys. Res. Lett.*, *34*, L24307, doi:10.1029/2007GL031067.

Moore, L. R., E. Gazel, R. Tuohy, A. S. Lloyd, R. Esposito, M. Steele-MacInnis, E. H. Hauri, P. J. Wallace, T. Plank, and R. J. Bodnar (2015), Bubbles matter: An assessment of the contribution of vapor bubbles to melt inclusion volatile budgets, *Am. Mineral.*, *100*, 806–823, doi:10.2138/am-2015-5036.

Newman, S., and J. B. Lowenstern (2002), VolatileCalc: A silicate melt–H2O–CO2 solution model written in Visual Basic for excel, *Comput. Geosci.*, *28*, 597–604.

Nicolas, A., I. Reuber and K. Benn (1988), A new magma chamber model based on structural studies in the Oman ophiolites, *Tectonophysics*, *151*, 87–105.

Niu, Y. (2004), Bulk-rock major and trace element compositions of abyssal peridotites: Implications for mantle melting, melt extraction and post-melting processes beneath mid-ocean ridges, *J. Petrol.*, *45*, 2423–2458, doi:10.1093/petrology/egh068.

O'Neill, H. S. C., and F. E. Jenner (2012), The global pattern of trace-element distributions in ocean floor basalts, *Nature*, *491*, 698–704, doi:10.1038/nature11678.

Paquet, M., M. Cannat, D. Brunelli, C. Hamelin, and E. Humler (2016), Effect of melt/mantle interactions on MORB chemistry at the easternmost Southwest Indian Ridge (61°–67° E), *Geochem. Geophys. Geosyst.*, *17*, 4605–4640, doi:10.1002/2016GC006385.

Perfit, M. R., and W. W. Chadwick (1998), Magmatism at mid-ocean ridges: Constraints from volcanological and geochemical investigations, in *Faulting and Magmatism at Mid-Ocean Ridges*, edited by W. Roger Buck et al., AGU, Washington, D. C., doi:10.1029/GM106p0059.

Perfit, M. R., D. Fornari, M. Smith, J. Bender, C. Langmuir, and R. Haymon (1994), Small-scale spatial and temporal variations in mid-ocean ridge crest magmatic processes, *Geology*, *22*, 375–379.

Phipps Morgan, J., and Y. Chen (1993), The genesis of oceanic crust: Magma injection, hydrothermal circulation, and crustal flow, *J. Geophys. Res.*, *98*, 6283–6297.

Quick, J., and R. Denlinger (1993), Ductile deformation and the origin of layered gabbro in ophiolites, *J. Geophys. Res.*, *98*, 14,015–14,027.

Reid, I., and H. R. Jackson (1991), Oceanic spreading rate and crustal thickness, *Mar. Geophys. Res.*, *5*, 165–172, doi:10.1007/BF00163477.

Rosenthal, A., E. H. Hauri, and M. M. Hirschmann (2015), Experimental determination of C, F, and H partitioning between mantle minerals and carbonated basalt, CO2/Ba and CO2/Nb systematics of partial melting, and the CO2 contents of basaltic source regions, *Earth Planet. Sci. Lett.*, *412*, 77–87, doi:10.1016/j.epsl.2014.11.044.

Rubin, K. H., and J. M. Sinton, (2007), Inferences on mid-ocean ridge thermal and magmatic structure from MORB compositions, *Earth Planet. Sci. Lett.*, *260*, 257–276, doi:10.1016/j.epsl.2007.05.035.

Rubin, K. H., J. M. Sinton, J. Maclennan, and E. Hellebrand (2009), Magmatic filtering of mantle compositions at mid-ocean-ridge volcanoes, *Nat. Geosci.*, *2*, 1–8. doi:10.1038/ngeo504.

Saal, A. E., E. H. Hauri, C. H. Langmuir, and P. R. Perfit (2002), Vapor undersaturation in primitive mid-ocean ridge basalt and the volatile content of the Earth's upper mantle, *Nature*, *419*, 451–455.

Sanfilippo, A., R. Tribuzio, and M. Tiepolo (2014), Mantle–crust interactions in the oceanic lithosphere: Constraints from minor and trace elements in olivine, *Geochim. Cosmochim. Acta*, *141*, 423–439, doi:10.1016/j.gca.2014.06.012

Shaw, A. M., M. D. Behn, S. E. Humphris, R. A. Sohn, and P. M. Gregg (2010), Deep pooling of low degree melts and volatile fluxes at the 85°E segment of the Gakkel Ridge: Evidence from olivine-hosted melt inclusions and glasses, *Earth Planet. Sci. Lett.*, *289*, 311–322, doi:10.1016/j.epsl.2009.11.018.

Shaw, W. J., and J. Lin (1996), Models of ocean ridge lithospheric deformation: Dependence on crustal thickness, spreading rate, and segmentation, *J. Geophys. Res.*, *101*, 17,977–17,993, doi:10.1029/96JB00949.

Shimizu, K., A. E. Saal, C. E. Myers, A. N. Nagle, E. H. Hauri, D. W. Forsyth, V. S. Kamenetsky, and Y. Niu (2016), Two-component mantle melting-mixing model for the generation of mid-ocean ridge basalts: Implications for the volatile content of the Pacific upper mantle, *Geochim. Cosmochim. Acta*, *176*, 44–80, doi:10.1016/j.gca.2015.10.033.

Shishkina, T. A., R. E. Botcharnikov, F. Holtz, R. R. Almeev, A. M. Jazwa, and A. A. Jakubiak (2014), Compositional and pressure effects on the solubility of H_2O and CO_2 in mafic melts, *Chem. Geol.*, *388*, 1–18, doi:10.1016/j.chemgeo.2014.09.001.

Simons, K., J. Dixon, J.-G. Schilling, R. Kingsley, and R. Poreda (2002), Volatiles in basaltic glasses from the Easter-Salas y Gomez Seamount Chain and Easter Microplate: Implications for geochemical cycling of volatile elements, *Geochem. Geophys. Geosyst.*, *3*(7), 1–29, doi:10.1029/2001GC000173.

Sims, K., S. Goldstein, J. Blichert-Toft, M. Perfit, P. Kelemen, D. Fornari, P. Michael, M. Murrell, S. Hart, and D. DePaolo (2002), Chemical and isotopic constraints on the generation and transport of magma beneath the East Pacific Rise, *Geochim. Cosmochim. Acta*, *66*, 3481–3504.

Singh, S., W. Crawford, H. Carton, and T. Seher (2006), Discovery of a magma chamber and faults beneath a Mid-Atlantic Ridge hydrothermal field, *Nature*, *442*, 1029–1032.

Sinton, J., and R. Detrick (1992), Mid-ocean ridge magma chambers, *J. Geophys. Res.*, *97*, 197–216.

Sleep, N. H. (1975), Formation of oceanic crust: Some thermal constraints, *J. Geophys. Res.*, *80*, 4037–4042.

Sleep, N. H., and J. M. Warren (2014), Effect of latent heat of freezing on crustal generation at low spreading rates, *Geochemistry*, *15*, 3161–3174, doi:10.1002/2014GC005423.

Soule, S. A., D. S. Nakata, D. J. Fornari, A. T. Fundis, M. R. Perfit, and M. D. Kurz (2012), CO2 variability in mid-ocean ridge basalts from syn-emplacement degassing: Constraints on eruption dynamics, *Earth Planet. Sci. Lett.*, *327–328*, 39–49, doi:10.1016/j.epsl.2012.01.034.

Sparks, D. W., and E. M. Parmentier (1991), Melt extraction from the mantle beneath spreading centers, *Earth Planet. Sci. Lett.*, *105*, 368–377, doi:10.1016/0012-821X(91)90178-K.

Standish, J. J., H. J. B. Dick, P. J. Michael, W. G. Melson, and T. O'Hearn (2008), MORB generation beneath the ultraslow spreading Southwest Indian Ridge (9–25°E): Major element chemistry and the importance of process versus source, *Geochem. Geophys. Geosyst.*, *9*, Q05004, doi:10.1029/2008GC001959.

Tormey, D., T. Grove, and W. Bryan (1987), Experimental petrology of normal MORB near the Kane Fracture Zone: 22–25 N, mid-Atlantic ridge, *Contrib. Mineral. Petrol.*, *96*, 121–139.

Villiger, S., O. Müntener, and P. Ulmer (2007), Crystallization pressures of mid-ocean ridge basalts derived from major element variations of glasses from equilibrium and fractional crystallization experiments, *J. Geophys. Res.*, *112*, B01202, doi:10.1029/2006JB004342.

Wallace, P. J., and J. Roberge (2004), Data report: Volatiles in submarine basaltic glasses from the Australian Antarctic Discordance (ODP Leg 187), edited by R. B. Pedersen, D. M. Christie, and D. J. Miller, *Proc. ODP, Sci. Results*, 187. [Available at http://www-odp.tamu.edu/publications/187_SR/207/207.htm.]

Wanless, V. D., and A. M. Shaw (2012), Lower crustal crystallization and melt evolution at mid-ocean ridges, *Nat. Geosci.*, *5*, 651–655, doi:10.1038/ngeo1552.

Wanless, V. D., M. R. Perfit, W. I. Ridley, and E. Klein (2010), Dacite petrogenesis on mid-ocean ridges: Evidence for oceanic crustal melting and assimilation, *J. Petrol.*, *51*, 2377–2410, doi:10.1093/petrology/egq056.

Wanless, V. D., M. R. Perfit, W. I. Ridley, P. J. Wallace, C. B. Grimes, and E. M. Klein (2011), Volatile abundances and oxygen isotopes in basaltic to dacitic lavas on mid-ocean ridges: The role of assimilation at spreading centers, *Chem. Geol.*, *287*, 54–65, doi:10.1016/j.chemgeo.2011.05.017.

Wanless, V. D., M. D. Behn, A. M. Shaw, and T. Plank (2014), Variations in melting dynamics and mantle compositions along the Eastern Volcanic Zone of the Gakkel Ridge: Insights from olivine-hosted melt inclusions, *Contrib. Mineral. Petrol.*, *167*, 1005, doi:10.1007/s00410-014-1005-7.

Wanless, V. D., A. M. Shaw, M. D. Behn, S. A. Soule, J. Escartin, and C. Hamelin (2015), Magmatic plumbing at Lucky Strike volcano based on olivine-hosted melt inclusion compositions, *Geochem. Geophys. Geosyst.*, *16*, 126–147, doi:10.1002/2014GC005517.

White, R., T. A. Minshull, M. J. Bickle, and C. J. Robinson (2001) Melt generation at very slow-spreading oceanic ridges: Constraints from geochemical and geophysical data, *J. Petrol.*, *42*, 1171–1196, doi:10.1093/petrology/42.6.1171.

White, W. M., and E. M. Klein (2014), Composition of the Oceanic Crust, in *Treatise on Geochemistry* 2nd ed., vol. 4, edited by H. D. Holland, and K. K. Turekian, pp. 457–496, Elsevier, Pergamon, Oxford, U. K., doi:10.1016/B978-0-08-095975-7.00315-6.

Witham, F., J. Blundy, S. C. Kohn, P. Lesne, and J. Dixon (2012), SolEx: A model for mixed COHSCl-volatile solubilities and exsolved gas compositions in basalt, *Comput. Geosci.*, *45*, 87–97, doi:10.1016/j.cageo.2011.09.021.

Workman, R. K., and S. R. Hart (2005), Major and trace element composition of the depleted MORB mantle (DMM), *Earth Planet. Sci. Lett.*, *231*, 53–72, doi:10.1016/j.epsl.2004.12.005.

Yang, H.-J., R. J. Kinzler, and T. L. Grove (1996), Experiments and models of anhydrous, basaltic olivine-plagioclase-augite saturated melts from 0.001 to 10 kbar, *Contrib. Mineral. Petrol.*, *124*, 1–18.